

Review

# Recent Advances in Electrochemical Sensors for Detecting Toxic Gases: NO<sub>2</sub>, SO<sub>2</sub> and H<sub>2</sub>S

Md Ashfaque Hossain Khan <sup>\*</sup>, Mulpuri V. Rao and Qiliang Li <sup>\*</sup>

Department of Electrical and Computer Engineering, George Mason University, Fairfax, VA 22030, USA; rmlpuri@gmu.edu

<sup>\*</sup> Correspondence: mkhan53@gmu.edu (M.A.H.K.); qli6@gmu.edu (Q.L.)

Received: 13 January 2019; Accepted: 14 February 2019; Published: 21 February 2019



**Abstract:** Toxic gases, such as NO<sub>x</sub>, SO<sub>x</sub>, H<sub>2</sub>S and other S-containing gases, cause numerous harmful effects on human health even at very low gas concentrations. Reliable detection of various gases in low concentration is mandatory in the fields such as industrial plants, environmental monitoring, air quality assurance, automotive technologies and so on. In this paper, the recent advances in electrochemical sensors for toxic gas detections were reviewed and summarized with a focus on NO<sub>2</sub>, SO<sub>2</sub> and H<sub>2</sub>S gas sensors. The recent progress of the detection of each of these toxic gases was categorized by the highly explored sensing materials over the past few decades. The important sensing performance parameters like sensitivity/response, response and recovery times at certain gas concentration and operating temperature for different sensor materials and structures have been summarized and tabulated to provide a thorough performance comparison. A novel metric, sensitivity per ppm/response time ratio has been calculated for each sensor in order to compare the overall sensing performance on the same reference. It is found that hybrid materials-based sensors exhibit the highest average ratio for NO<sub>2</sub> gas sensing, whereas GaN and metal-oxide based sensors possess the highest ratio for SO<sub>2</sub> and H<sub>2</sub>S gas sensing, respectively. Recently, significant research efforts have been made exploring new sensor materials, such as graphene and its derivatives, transition metal dichalcogenides (TMDs), GaN, metal-metal oxide nanostructures, solid electrolytes and organic materials to detect the above-mentioned toxic gases. In addition, the contemporary progress in SO<sub>2</sub> gas sensors based on zeolite and paper and H<sub>2</sub>S gas sensors based on colorimetric and metal-organic framework (MOF) structures have also been reviewed. Finally, this work reviewed the recent first principle studies on the interaction between gas molecules and novel promising materials like arsenene, borophene, blue phosphorene, GeSe monolayer and germanene. The goal is to understand the surface interaction mechanism.

**Keywords:** gas sensor; nitrogen dioxide (NO<sub>2</sub>); sulphur dioxide (SO<sub>2</sub>); hydrogen sulfide (H<sub>2</sub>S); density-functional theory (DFT); Internet of Things (IoT); sensitivity; response/recovery time

---

## Contents

1. Introduction
2. Recent Advances in NO<sub>2</sub> Gas Detection
  - 2.1. Graphene and Its Derivatives-Based NO<sub>2</sub> Sensors
  - 2.2. Transition Metal Dichalcogenide (TMD)-Based NO<sub>2</sub> Sensors
  - 2.3. Metal and Metal-Oxide Nanostructure-Based NO<sub>2</sub> Sensors
  - 2.4. GaN-Based NO<sub>2</sub> Sensors
  - 2.5. Organic Materials-Based NO<sub>2</sub> Sensors
  - 2.6. Hybrid Materials-Based NO<sub>2</sub> Sensors

3. Recent Advances in SO<sub>2</sub> Gas Detection
  - 3.1. Carbon Material-Based SO<sub>2</sub> Sensors
  - 3.2. Metal and Metal-Oxide Nanostructures-Based SO<sub>2</sub> Sensors
  - 3.3. GaN-Based SO<sub>2</sub> Sensors
  - 3.4. Solid Electrolyte-Based SO<sub>2</sub> Sensors
  - 3.5. Zeolite-Based SO<sub>2</sub> Sensors
  - 3.6. Paper-Based SO<sub>2</sub> Sensors
4. Recent Advances in H<sub>2</sub>S Gas Detection
  - 4.1. Carbon Material-Based H<sub>2</sub>S Sensors
  - 4.2. GaN-Based H<sub>2</sub>S Sensors
  - 4.3. Metal and Metal Oxide-Based H<sub>2</sub>S Sensors
    - 4.3.1. Nanostructured Metal Oxide-Based Sensors
    - 4.3.2. Mesoporous Metal Oxide-Based Sensors
    - 4.3.3. Metal Oxide Microsphere-Based Sensors
  - 4.4. MOF-Based H<sub>2</sub>S Sensors
  - 4.5. Organic Materials-Based H<sub>2</sub>S Sensors
  - 4.6. Solid Electrolytes-Based H<sub>2</sub>S Sensors
5. Recent Density-Functional Theory (DFT) Study of Gas Molecule-Sensor Interaction
6. Calibration of Toxic Gas Sensors
7. Toxic Gas Sensors in Internet of Things (IoT) Applications
8. Future Perspectives and Conclusions

Acknowledgments

Conflicts of Interest

References

## 1. Introduction

Humans are exposed to various air toxins in the indoor and outdoor environment. Poor air quality is a well-known trigger for various health problems which can often result in life threatening and expensive emergency care. Therefore, precise toxic gas sensing will not only bring a major benefit to industries but also to day-to-day life for all people. Nitrogen dioxide (NO<sub>2</sub>) is one of the common toxic air pollutants, which is mostly found as a mixture of nitrogen oxides (NO<sub>x</sub>) with different ratios (x). NO<sub>2</sub> is a reddish-brown, irritant, toxic gas having a characteristic sharp and biting odor. The LC<sub>50</sub> (the lethal concentration for 50% of those exposed) for one hour of NO<sub>2</sub> exposure for humans has been estimated as 174 ppm. The major sources of NO<sub>2</sub> are from combustion of fuels such as certain coals and oil [1], biomass burning due to the extreme heat of lightning during thunderstorms [2], and nitrogen fixation by microorganisms due to agricultural fertilization [3]. The noteworthy impacts of NO<sub>2</sub> include: respiratory inflammation of the airways, decreased lung function due to long term exposure, increased risk of respiratory conditions [4,5], increased responsiveness to allergens, contribution to the formation of fine particulate matter (PM) and ground level ozone which have adverse health effects, and contribution to acid rain causing damage to vegetation, buildings and acidification of lakes and streams [6,7].

Sulphur dioxide (SO<sub>2</sub>) is the most common air pollutant, mostly found as a mixture of sulfur oxides (SO<sub>x</sub>). It is an invisible gas with a nasty, sharp smell. The maximum concentration for SO<sub>2</sub> exposures of 30 min to 1 h has been estimated as 50 to 100 ppm. The main sources of SO<sub>2</sub> include burning of fossil fuels (fuel oil, coal) in power stations, oil refineries, other large industrial plants, motor vehicles and domestic boilers [8,9]. It is also produced from natural sources like active volcanoes

and forest fires. When mineral ores containing sulfur are processed,  $\text{SO}_2$  is released to atmosphere as well. Excessive exposure of  $\text{SO}_2$  causes harms on the eye, lung and throat [10,11]. It is toxic to some plants, inducing visible signs of injury and reducing yields.  $\text{SO}_2$  gas combined with air moisture causes gradual damage to some building materials (e.g., limestone).  $\text{SO}_2$  can readily dissolve in the water droplets in clouds, causing acid rain that affects natural balance of rivers, lakes and soils, resulting in damage to wildlife and vegetation.

Hydrogen sulfide ( $\text{H}_2\text{S}$ ) is a highly toxic, malodorous, intensely irritating gas. The maximum concentration for  $\text{H}_2\text{S}$  exposure for one hour without grave after-effects has been estimated as 170 to 300 ppm. The key sources of  $\text{H}_2\text{S}$  gas are from decaying organic materials, natural gas, volcanic gas, petroleum, sewage plants and sulfur deposits [12,13]. Minimal exposure to  $\text{H}_2\text{S}$  gas causes nose/eye irritation, olfactory nerve paralysis. Moderate amount may cause sore throat, cough, keratoconjunctivitis, chest tightness and pulmonary edema. Excessive exposure causes headaches, disorientation, loss of reasoning, coma, convulsions and even death [14,15].

In comparison to gas detection techniques like optical [16], acoustic [17] and gas chromatographic methods [18], electrochemical sensing is the most popular technique for ambient toxic gas monitoring. The key advantages of electrochemical detection are having low energy linear output with high resolution, good selectivity and repeatability, ppm level detection with high accuracy, and being more inexpensive than other techniques [19]. However, electrochemical sensors are highly sensitive to temperature fluctuations and have minimal shelf life. The operating temperature should be kept as steady as possible to get the best sensor performances. Sensors with high operating temperature are generally employed in industrial and space applications. Over the last decades, research on toxic gas sensing was mostly focused on using electrochemical sensors which were built from various functional materials, such as carbon nanomaterials [20–31], metal oxide/metallic nanostructures [32–38], transition metal dichalcogenides (TMDs) [39–41], gallium nitride (GaN) [42–45], organic materials [46–50], solid electrolytes [51–54], zeolites [55–58] and others [59–63]. Recently numerous research efforts have been made on suitable gas sensing materials to detect nitrogen oxides, sulfur oxides and hydrogen sulfide gases. In this work, we have reviewed the recent advances in electrochemical sensors for toxic gas detection focusing mainly on  $\text{NO}_2$ ,  $\text{SO}_2$  and  $\text{H}_2\text{S}$  gas sensors. The recent progress of each of these toxic gas detections has been categorized based on various sensing materials of high interest. The goal is to shine a light on the future development trend of toxic gas detection, a vital technology for the emerging Internet of Things era.

## 2. Recent Advances in $\text{NO}_2$ Gas Detection

### 2.1. Graphene and Its Derivatives-Based $\text{NO}_2$ Sensors

Graphene provides a large surface area, atom-thick 2D conjugated structures, low electrical noise, high conductivity, and excellent electronic properties [64]. Having high surface-to volume ratio, reduced graphene oxide (RGO) provides large surface areas, defects and low electrical noise as well [65]. All these characteristics make both graphene and RGO suitable candidates for gas adsorption and detection.

Recently epitaxial graphene has been utilized to detect ppb levels of  $\text{NO}_2$  gas and it was found that single-layer graphene is superior to bilayer graphene in terms of carrier concentration response [66]. Wang et al. [67] incorporated Pd nanoparticles (NPs) and  $\text{SnO}_2$  NPs on reduced graphene oxide to form Pd- $\text{SnO}_2$ -RGO hybrids as  $\text{NO}_2$  gas sensing materials. A high resolution transmission electron microscopy (HR-TEM) image of Pd- $\text{SnO}_2$ -RGO reveals that 3–5 nm sized nanoparticles (NPs) are deposited on RGO nanosheets (Figure 1A). Lattice distances of 0.33 nm and 0.23 nm indicated the presence of  $\text{SnO}_2$  NPs and Pd NPs, respectively. When a Pd- $\text{SnO}_2$ -RGO nanosheet was exposed to 1 ppm of  $\text{NO}_2$  gas at room temperature, a response of 3.92 was obtained with a response time of 13 s which are better compared to RGO as well as  $\text{SnO}_2$ -RGO hybrids. However, the recovery time (105 s) was slower due to addition of Pd NPs. To perform a concentration response test, the fabricated

sensor was exposed to 50 ppb to 2 ppm of  $\text{NO}_2$  gas. The sensor showed an increasing response trend with  $\text{NO}_2$  concentration (Figure 1B). The selectivity response of the Pd-SnO<sub>2</sub>-RGO sensor was examined towards  $\text{Cl}_2$ , NO and some common volatile organic compounds (VOCs). Results indicated that the Pd-SnO<sub>2</sub>-RGO hybrid is highly selective to  $\text{NO}_2$  gas (Figure 1C). Preferred adsorption sites providing for  $\text{NO}_2$ , high conductivity and the catalytic properties of Pd NPs are mainly responsible for the sensing performance improvement. However, no sulfur-containing gas was included in the test interference gases. Since Pd is known to interact strongly with S [68], the fabricated sensor should have been tested with S-containing gases to get the complete selectivity test picture. The same Wang et al. group [69] experimented with the introduction of oxygen vacancies (OV) into reduced graphene oxide nanosheets decorated with SnO<sub>2</sub> nanoparticles (NPs). OVs enhance the adsorption of O<sub>2</sub> molecules which in turn enhances the adsorption of  $\text{NO}_2$  molecules onto SnO<sub>2</sub> NPs. Upon exposure to 1 ppm of  $\text{NO}_2$  gas, the SnO<sub>2</sub>-RGO-OVs-based sensor showed a response of 3.80 with reasonable response and recovery time. These  $\text{NO}_2$  sensing performances are better than those of other previously reported RGO-based sensors.

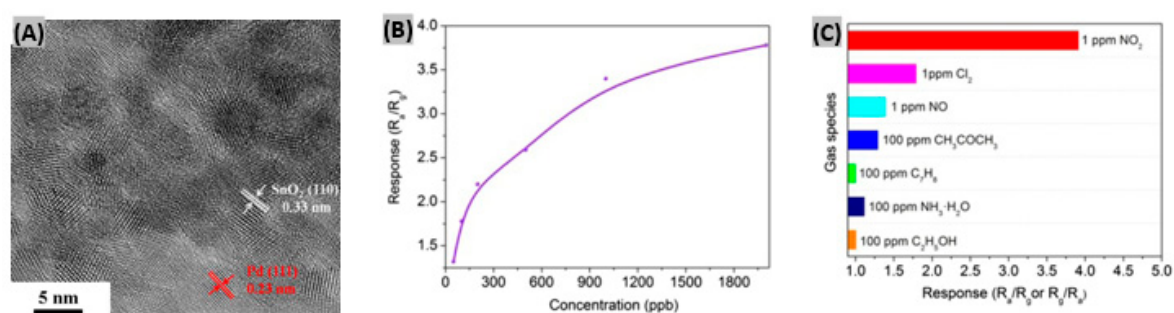


**Figure 1.** (A) HR-TEM image of fabricated Pd-SnO<sub>2</sub>-RGO hybrid. (B) Sensor response toward different concentrations of  $\text{NO}_2$  gas at room temperature. (C) The response of the sensor to  $\text{Cl}_2$ , NO,  $\text{NO}_2$ , acetone, toluene, ammonia and ethanol in a selectivity test. Figures adapted with permission from [67], Copyright 2018 Elsevier.

In another study, Akbari et al. [70] decomposed methane in an arc discharge experiment to get carbonaceous materials (C-strands) between graphite electrodes. Upon  $\text{NO}_2$  exposure, the conductivity of the fabricated C strands was altered due to charge transfer between the carbon film and  $\text{NO}_2$  molecules. Previously, Zhang et al. [71] reported a rGO/Au nanocomposite-based  $\text{NO}_2$  sensor using a hydrothermal treatment. It provided good sensitivity with a quick response–recovery process at 50 °C.

## 2.2. Transition Metal Dichalcogenide (TMD)-Based $\text{NO}_2$ Sensors

Two-dimensional (2D) transition metal dichalcogenides (TMDs) possess semiconducting nature, high surface-to-volume ratio and atomically thin-layered structures which are useful properties required to be a convincing sensing material [72]. MoS<sub>2</sub>, WS<sub>2</sub>, ReS<sub>2</sub>, MoSe<sub>2</sub>, MoTe<sub>2</sub>, WSe<sub>2</sub> and ReSe<sub>2</sub> are very promising 2D TMDs for gas sensing purposes [73–75]. Agrawal et al. prepared in-plane and edge-enriched p-MoS<sub>2</sub> flakes (mixed MoS<sub>2</sub>) to detect  $\text{NO}_2$  gas at room temperature [76]. A FE-SEM image of the mixed MoS<sub>2</sub> flakes is shown in Figure 2A. The blackish region represents the in-plane MoS<sub>2</sub> flakes and the white region represents the edge-enriched MoS<sub>2</sub> flakes. Most likely, the edge-enriched MoS<sub>2</sub> flakes are white due to their height from the substrate surface. Figure 2B displays a sensitivity vs.  $\text{NO}_2$  concentration bar graph at RT and 125 °C.  $\text{NO}_2$  is an electron acceptor and it withdraws electrons from the MoS<sub>2</sub> flakes, thus causing the resistance decrease of the mixed MoS<sub>2</sub> flake-based sensor. The response and recovery time of the sensor were better at 125 °C than at RT. This happened because the adsorption energy of the  $\text{NO}_2$  gas molecule with the MoS<sub>2</sub> flakes is very high at RT. The sensitivity of the sensor had been enhanced under UV light illumination as shown in Figure 2C. This improvement is attributed to the photoactivated desorption of adsorbed oxygen and creation of fresh active sites on the edges of MoS<sub>2</sub> flakes. In another study, Kumar et al. [77] prepared a 1D

MoS<sub>2</sub> nanowire network which showed a detection limit of 4.6 ppb NO<sub>2</sub> with good sensitivity. At the estimated optimum operating temperature (60 °C), response and recovery times were found as 16 s and 172 s, respectively, at 5 ppm NO<sub>2</sub> exposure. Previously, Choi et al. [78] introduced Nb atoms into 2D MoSe<sub>2</sub> host films. Figure 2D displays the low magnification planar annular dark-field scanning transmission electron microscopy (ADF-STEM) images and FFT patterns (inset) of MoSe<sub>2</sub>: Nb 1C, where 1C indicates one deposition cycle in the plasma-enhanced atomic layer deposition (PEALD) process. The polycrystal ring patterns in the image represent the presence of a few grains. Variably Nb-doped MoSe<sub>2</sub> sensor films were exposed to different NO<sub>2</sub> concentrations as shown in Figure 2E. The highest gas response was found for a MoSe<sub>2</sub>:Nb 1C device among the three tested devices because at low Nb dopant concentrations, MoSe<sub>2</sub> showed an improved NO<sub>2</sub> gas response due to its small grains and stabilized grain boundaries. At high Nb dopant concentrations, the NO<sub>2</sub> gas response was degraded due to the increase of gas-unresponsive metallic NbSe<sub>2</sub> regions, so an optimum Nb concentration is required for achieving a better gas response. The resistance of the MoSe<sub>2</sub>-based sensor gradually increased due to oxidation, whereas the Nb-doped MoSe<sub>2</sub> sensor showed very stable response (Figure 2F). This means, introduction of Nb atoms onto 2D layered MoSe<sub>2</sub> promotes a stable gas response and the long-term stability of the sensor. Also, a significant enhancement in sensing response with quick response-recovery toward NO<sub>2</sub> was observed on WS<sub>2</sub> nanosheet functionalized with Ag NWs [79].

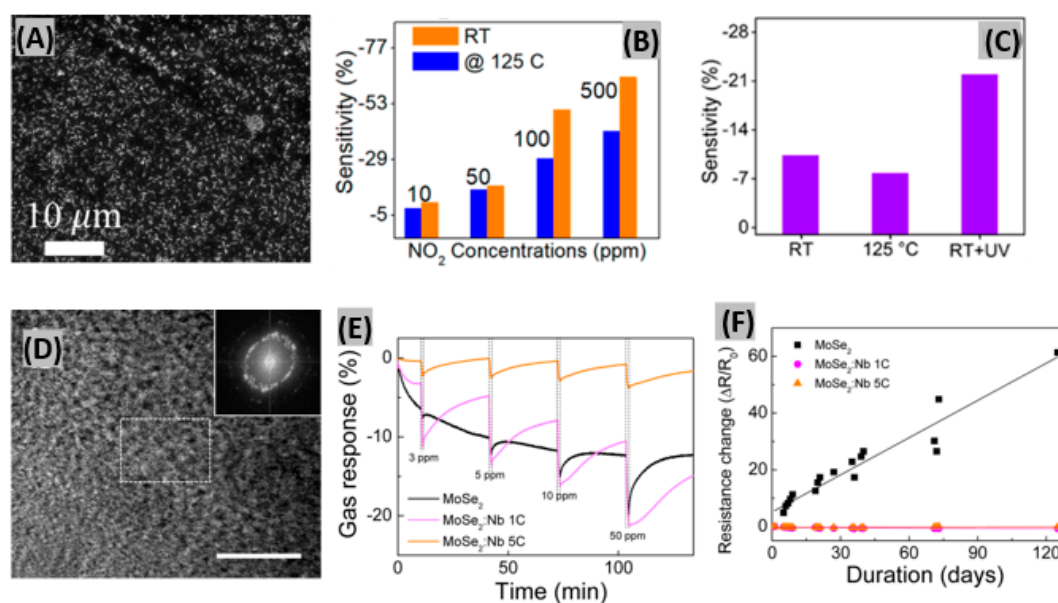


**Figure 2.** (A) FE-SEM image of the mixed MoS<sub>2</sub> flakes. (B) Sensitivity vs. NO<sub>2</sub> concentration bar graph at RT and 125 °C. (C) Sensitivity bar graph of the mixed MoS<sub>2</sub> flakes-based sensor for a NO<sub>2</sub> gas concentration of 10 ppm. Figures adapted with permission from [76], Copyright 2018 American Chemical Society. (D) Planar ADF-STEM image of the MoSe<sub>2</sub>:Nb 1C film (white scale bar = 10 nm). Inset shows the corresponding FFT patterns. (E) Percent gas response for MoSe<sub>2</sub>, MoSe<sub>2</sub>:Nb 1C, and MoSe<sub>2</sub>:Nb 5C sensors at 3 to 50 ppm of NO<sub>2</sub> gas. (F) Response of the MoSe<sub>2</sub>, MoSe<sub>2</sub>:Nb 1C, and MoSe<sub>2</sub>:Nb 5C sensors over 120 days. Figures adapted with permission from [78], Copyright 2017 American Chemical Society.

### 2.3. Metal and Metal-Oxide Nanostructure-Based NO<sub>2</sub> Sensors

Metal oxides can be synthesized in various nanostructure morphologies like nanowires, nanoparticles, nanotubes, nanoflowers, nanocomposites and nanosheets for the enhancement of sensing performance [80–82]. Besides, porosity and permeable shell layers contribute to absolute electron depletion and gas diffusion that allow sensor devices to achieve high sensitivity toward gases [83]. Qiang et al. reported a NO<sub>2</sub> gas sensor based on porous silicon (PS)/WO<sub>3</sub> nanorods (NRs)

functionalized with Pd NPs [84]. PS WO<sub>3</sub> NRs were synthesized by electrochemical methods and thermal oxidation of W film, respectively. Pd NPs were deposited onto WO<sub>3</sub> NRs, by the reduction of a Pd complex solution. Three different samples of PS/WO<sub>3</sub> NRs–Pd NPs were prepared by varying the amount of Pd NPs on the substrate. These are PS/WO<sub>3</sub>–Pd20, PS/WO<sub>3</sub>–Pd40 and PS/WO<sub>3</sub>–Pd60, where the order of the amount of Pd NPs is Pd60 > Pd40 > Pd20. A TEM image of PS/WO<sub>3</sub>–Pd60 displays the agglomeration of Pd NPs on WO<sub>3</sub> NRs (Figure 3A). Gas concentration tests on the PS/WO<sub>3</sub>–Pd60 sensor revealed a ppb level detection capacity at RT with a faster response time (Figure 3B). The catalytic activity of Pd NPs enhanced the NO<sub>2</sub> molecule adsorption and thereby enhanced the sensor response, so a PS/WO<sub>3</sub>–Pd60 sensor having the highest amount of Pd NPs showed the highest sensor response at room temperature (Figure 3C). With a facile fabrication process and being compatible with the planar processes of the microelectronics industry, ultra-thin PdO films provided good sensing performances toward NO<sub>2</sub> [85], but they require a long recovery period (600–700 s) because of the lack of immediate interaction between NO<sub>2</sub> molecules and oxygen molecules adsorbed on sensor material surface. Also, ZnO nanostructured films obtained by a thermal evaporation method offered significantly enhanced response (622 at 100 ppm NO<sub>2</sub>) with good response-recovery at 200 °C [86]. The microwave-synthesized NiO film has been found to operate using ultra-low power of 0.2 μW at room temperature. It achieved a response of 4991% to 3 ppm NO<sub>2</sub> along with fast response-recovery [87]. Moreover, a reasonable sensor response toward low concentration of NO<sub>2</sub> was exhibited by the multicomponent oxide CuBi<sub>2</sub>O<sub>4</sub> at 400 °C [88]. Recently, Hung et al. synthesized three sensors of ZnO (Z2, Z4 and Z6) and Zn<sub>2</sub>SnO<sub>4</sub> (ZS2, ZS4 and ZS6) NWs on microelectrode chips at 2, 4 and 6 cm from the thermal evaporation source, respectively [89]. It was found that the distance between the source and substrate strongly affected the gas response of the Zn<sub>2</sub>SnO<sub>4</sub> NW sensors. Figure 3D,E show FESEM images of the on-chip grown ZnO (Z2) NW and Zn<sub>2</sub>SnO<sub>4</sub> (ZS2) NW respectively.

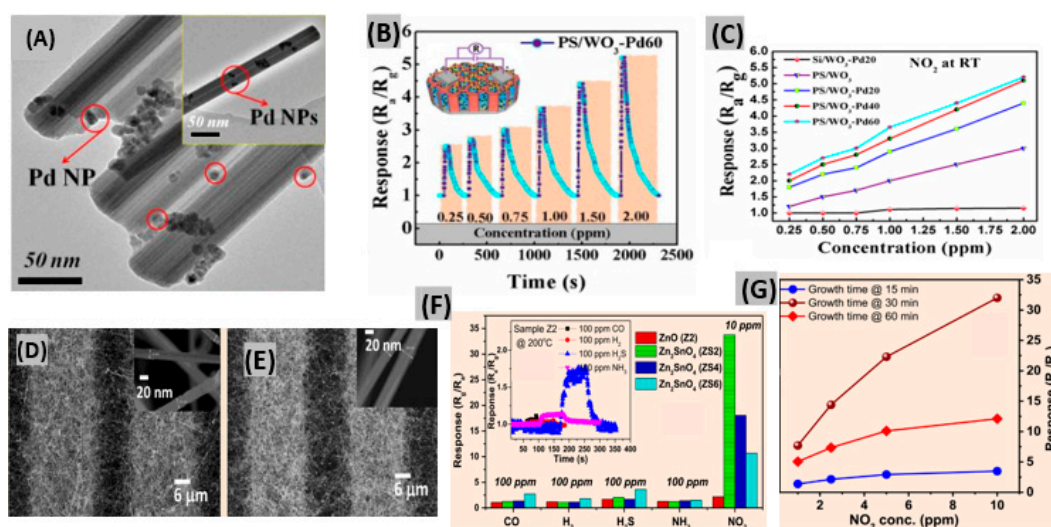


**Figure 3.** (A) TEM images of PS/WO<sub>3</sub>–Pd60 (inset shows a single PS/WO<sub>3</sub>–Pd60 NR). (B) Sensor response of PS/WO<sub>3</sub>–Pd60 to different concentrations of NO<sub>2</sub> at RT. (C) Response of Si/WO<sub>3</sub>–Pd20, PS/WO<sub>3</sub>, PS/WO<sub>3</sub>–Pd20, PS/WO<sub>3</sub>–Pd40 and PS/WO<sub>3</sub>–Pd60 sensors at different NO<sub>2</sub> concentrations. Figures adapted with permission from [84], Copyright 2018 MDPI. (D,E) FESEM images of on-chip grown ZnO and Zn<sub>2</sub>SnO<sub>4</sub> NWs. (F) Response comparison of Z2, ZS2, ZS4, ZS6 to 100 ppm CO, H<sub>2</sub>, H<sub>2</sub>S, NH<sub>3</sub> and 10 ppm NO<sub>2</sub>. (G) Sensor responses of the devices with growth times of 15 min, 30 min and 60 min as a function of NO<sub>2</sub> concentrations. Figures adapted with permission from [89], Copyright 2018 Elsevier.

The sensing performances of ZnO and Zn<sub>2</sub>SnO<sub>4</sub> NW sensors to NO<sub>2</sub> and other reducing gases are displayed in Figure 3F. Zn<sub>2</sub>SnO<sub>4</sub> NW exhibited significantly better response towards NO<sub>2</sub> gas in comparison to ZnO NW. Also, ZS2 showed higher response than ZS4 and ZS6, because placing the

sensors far from the source resulted in several surface defects due to the lack of a Sn source. Responses for  $\text{Zn}_2\text{SnO}_4$  NW sensors with growth times of 15, 30 and 60 min are shown in Figure 3G. It is revealed that comparatively high or low density of NWs decreases the gas response.

#### 2.4. GaN-Based $\text{NO}_2$ Sensors

Having a wide bandgap energy (3.4 eV), gallium nitride (GaN) is found to support higher peak internal electric fields than silicon or gallium arsenide (GaAs). This wide bandgap causes lower thermal electron-hole pair generation, hence allowing high working temperatures. GaN is less vulnerable to attack in caustic environments, and resistant to radiation because of the larger cohesion energies among its constituent atoms [90–93]. Bishop et al. proposed a double Schottky junction gas sensor based on BGaN/GaN [94]. Two devices were developed; first, 10 periods of 20 nm thick undoped GaN, and 20 nm thick BGaN formed the BGaN/GaN superlattice structure. Then a circular diode having 300  $\mu\text{m}$  as diameter was made with a 200  $\mu\text{m}$  spacing between two Pt contacts on the n-type GaN sample (Figure 4A). When the sensors were exposed to 450 ppm  $\text{NO}_2$  gas at different temperatures, BGaN/GaN SL sensor exhibited higher current change and sensitivity than GaN monolayer sensors (Figure 4B). This enhancement is caused by two main reasons: firstly, BGaN has more interface traps than GaN, which creates more adsorption sites at the interface for gas molecules resulting a greater SBH change. Secondly, BGaN shows columnar growth thus a decrease in the volume-to-area ratio at the interface that provides more interface traps within a given area. It was found that at higher temperatures and concentrations, saturation of the signal change leads to a nonlinear response for the BGaN/GaN SL resulting into a decrease in the responsivity of the device (Figure 4C). In another study, an AlGaN/GaN high electron mobility transistor (HEMT) with Pt functionalized gate demonstrated a high sensitivity of 38.5% toward 900 ppm  $\text{NO}_2$  at high operating temperature of 600  $^\circ\text{C}$  [95]. The fabricated heterostructure sensor exhibited robustness under severe environmental conditions with a very quick response time of 1 s. When sensors are integrated in chips, low power sensor operation is required. Lim et al. [96] made  $\text{SnO}_2$  sensitized AlGaN/GaN sensor operating at ultra-low power without using any heater. The fabricated sensor exhibited ppb level detection as well as fast response times.

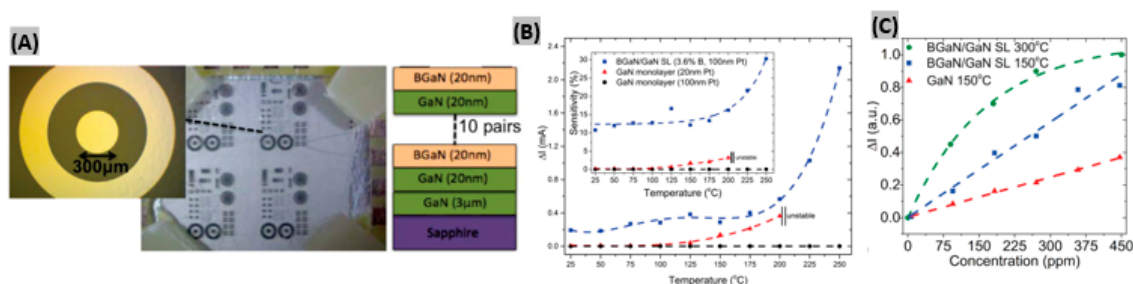


**Figure 4.** (A) Fabricated BGaN/GaN SL and GaN devices. (B) Current change and Sensitivity (Inset) of BGaN/GaN SL and GaN sensors to 450 ppm  $\text{NO}_2$  at 5 V bias at different temperatures. (C) Sensor current changes vs.  $\text{NO}_2$  concentrations for various temperatures. Figures adapted with permission from [94], Copyright 2015 AIP Publishing LLC.

#### 2.5. Organic Materials-Based $\text{NO}_2$ Sensors

Conducting and semiconducting organic films are promising gas sensing materials due to their excellent ability of tuning the chemical and physical properties on exposure to gas molecules. Also, recognition groups can be integrated covalently on organic sensing materials in order to get high selectivity and response [97]. Organic field effect transistors (OFETs) and thin film transistors (TFTs) are two major forms of organic material-based sensors. Kumar et al. [98] synthesized an OFET to detect  $\text{NO}_2$  gas using gate bias as control unit. The active layer of the OFET was the polymer poly [N-90-heptadecanyl-2,7-carbazole-alt-5,5-(40,70-di-2-thienyl-20,10,30-benzothiadiazole]

(PCDTBT). The electron removal of  $\text{NO}_2$  molecule from the p-type conducting polymer PCDTBT led to an increase of conductivity. The typical transfer and output characteristics of OFET sensor are shown in Figure 5A,B, respectively. From the attained transfer and output characteristics, the mobility ( $\mu_{\text{sat}}$ ) and threshold voltage ( $V_{\text{th}}$ ) were obtained as  $1.13 \times 10^{-4} \text{ cm}^2 \text{ V}^{-1} \text{ s}^{-1}$  and  $-9 \text{ V}$ . From the gas concentration test, as shown in Figure 5C, the response increases linearly up to 10 ppm of exposure and then the increasing trend drops at higher concentrations. This happens because most of the active adsorption sites of the active PCDTBT layer get populated by  $\text{NO}_2$  molecules. The response and recovery time of the sensor at 1 ppm of  $\text{NO}_2$  exposure were obtained as shown in the inset of Figure 5C. The selectivity of the sensor upon exposure 10 ppm of different toxic gases was studied. Figure 5D displays that the OFET sensor exhibits the highest selectivity towards  $\text{NO}_2$  gas. Although the  $\text{H}_2\text{S}$  gas response was moderate, the recovery was incomplete. In another study, a 6,13-bis(triisopropylsilylethynyl)-pentacene (TIPS-pentacene) film-based  $\text{NO}_2$  sensor attained a sensitivity above 1000%/ppm along with quick response-recovery [99]. It was predicted that the high sensing performance is attributable to the effective charge transport on the top of low original carrier concentration. Huang et al. [100] fabricated TFTs using copper phthalocyanine (CuPc) for  $\text{NO}_2$  gas detection. The gate dielectric used here is a UV-ozone (UVO)-treated polymer. Figure 5E shows sensitivities of the TFT biased at  $V_{\text{D}} = V_{\text{G}} = -40 \text{ V}$  toward different  $\text{NO}_2$  concentrations and UVO treatment times ( $t_{\text{UVO}}$ ). It is seen that the sensitivity enhances significantly for sensors with longer  $t_{\text{UVO}}$  at all  $\text{NO}_2$  gas concentrations because of UVO-derived hydroxylated species on the dielectric surface. Gas selectivity tests revealed that without UVO treatment of the dielectric, the sensors are not at all selective to  $\text{NO}_2$  gas. However, at  $t_{\text{UVO}} = 360 \text{ s}$ , the sensitivity increased from 10% to almost 600% at a concentration of 20 ppm  $\text{NO}_2$  which is six times more sensitive than all other test gases (Figure 5F).

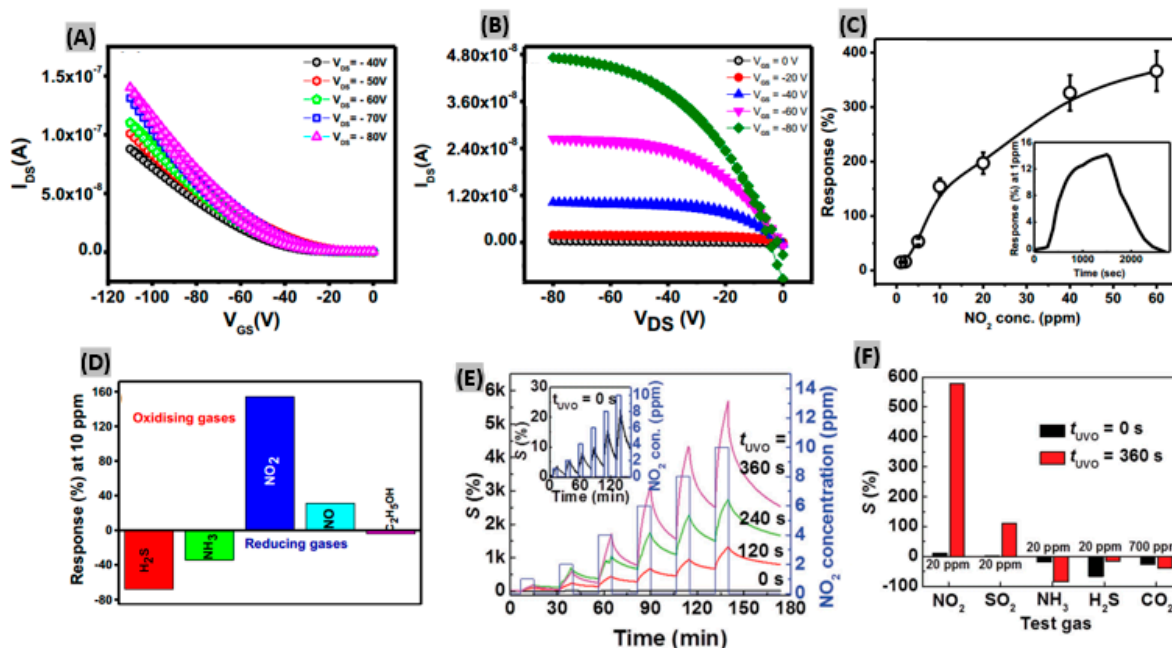


**Figure 5.** (A) Transfer (B) Output characteristics of the PCDTBT based OFET. (C) Sensor response at different  $\text{NO}_2$  concentrations. Response-recovery of the sensor at 1 ppm of  $\text{NO}_2$  (inset). (D) Selectivity graph of the sensor towards various analytes. Figures adapted with permission from [98], Copyright 2018 Elsevier. (E) Sensitivity profile at different  $\text{NO}_2$  concentrations and with UVO treatment times ( $t_{\text{UVO}}$ ). Inset shows the sensitivity at  $t_{\text{UVO}} = 0 \text{ s}$ . (F) Sensitivities obtained for TFT sensors with  $t_{\text{UVO}} = 0$  and 360 s at 20 ppm  $\text{NO}_2$ ,  $\text{SO}_2$ ,  $\text{NH}_3$ ,  $\text{H}_2\text{S}$  and 700 ppm  $\text{CO}_2$ . Figures adapted with permission from [100], Copyright 2017 WILEY-VCH Verlag GmbH & Co. KGaA, Weinheim.

## 2.6. Hybrid Materials-Based NO<sub>2</sub> Sensors

In most cases hybrid materials combine and exhibit the useful characteristics of their constituent materials to promote high sensing performances. For instances, both MoS<sub>2</sub> and RGO show good conductivity changes upon adsorption of NO<sub>2</sub> molecules, and thus a combination of MoS<sub>2</sub> and RGO results in high performance NO<sub>2</sub> gas sensors [101]. Recently, Wang et al. synthesized a MoS<sub>2</sub> nanoparticles-incorporated RGO hybrid material for NO<sub>2</sub> detection by a two-step wet-chemical method [102]. In the first step, powdered MoS<sub>2</sub> NPs were prepared by a modified liquid exfoliation method. Next, self-assembly of MoS<sub>2</sub> NPs and GO nanosheets, and hydrothermal treatment provided MoS<sub>2</sub>-RGO hybrid nanosheets. A high magnification SEM image of MoS<sub>2</sub>-RGO hybrids, shown in Figure 6A, reveals the presence of NPs on the RGO surface. It was found that the response time and recovery time decrease with increasing operating temperature while the sensor responses to NO<sub>2</sub> remain almost unchanged. The optimum operating temperature was obtained as 160 °C. A response-recovery curve to 3 ppm NO<sub>2</sub> gas at 160 °C is illustrated in Figure 6B. When the fabricated MoS<sub>2</sub>-RGO based sensor was exposed to NO<sub>2</sub> gas concentrations ranging from 100 ppb to 3 ppm, the response followed an increasing trend due to the increased amount of NO<sub>2</sub> molecules absorbed (Figure 6C). Wang et al. [103] synthesized a hybrid sensing material made of ZnO and poly(3-hexylthiophene) for the detection of NO<sub>2</sub> at room temperature. The fabricated nanosheet-nanorod structured bilayer film sensor showed a sensitivity of 180% at 50 ppm of gas exposure.

The sensing performance metrics like sensitivity/response, response and recovery times at certain gas concentration and operating temperatures, and sensitivity per ppm/response time ratio for different NO<sub>2</sub> sensor materials and structures are summarized in Table 1. It provides a brief comparative performances outline among different NO<sub>2</sub> sensor reported in recent years.

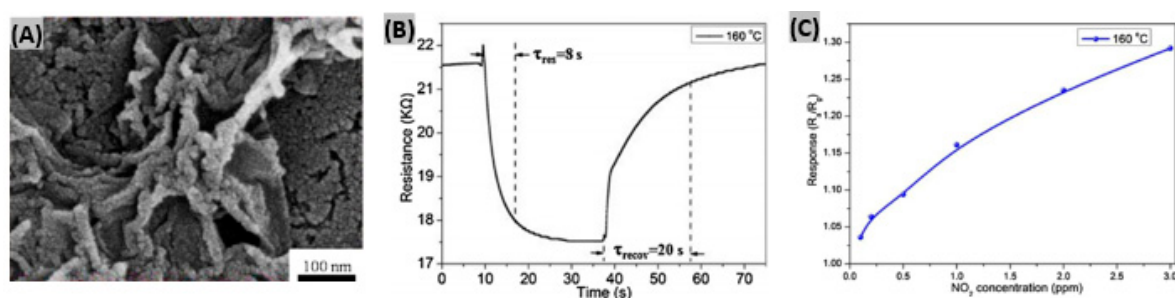


**Figure 6.** (A) High magnification SEM images of the fabricated MoS<sub>2</sub>-RGO hybrids. (B) Response-recovery curve of MoS<sub>2</sub>-RGO sensor to 3 ppm NO<sub>2</sub> at 160 °C. (C) Sensor responses to different NO<sub>2</sub> concentrations at 160 °C. Figures adapted with permission from [102], Copyright 2017 Elsevier.

**Table 1.** Gas sensing properties of recently developed NO<sub>2</sub> gas sensors.

Materials	Structure	Operating Temperature (°C)	Concentration (ppm)	Sensitivity/Response	Response Time (s)	Recovery Time (s)	Sensitivity per ppm Response time
SnO <sub>2</sub> /NRGO [104]	Nanosheets	RT	5	1.38	45	168	0.006
Graphene-SnO <sub>2</sub> [105]	Nanocomposites	150	1	24.7	175	148	0.14
SnO <sub>2</sub> /graphene [106]	Nanocomposites	150 °C	5	26,342	13	Long	405
		RT		171	7 min		0.081
RGO-polythiophene [107]	Thin film	RT	10	26.36	<180	<200	0.015
Ion-Beam Irradiated SnO <sub>2</sub> [108]	Nanowire	150	2	14.2	292	228	0.025
MoS <sub>2</sub> [109]	Flakes	RT (UV)	100	27.92	29	350	0.01
	Flakes	100	100	21.56	71	310	0.003
Hierarchical ZnO-RGO [110]	Nanosheets	100	0.05	12	306	450	0.78
MoS <sub>2</sub> /Graphene [111]	Aerogel	200 (microheater)	0.5	9.1	21.6	29.4	0.84
SnO <sub>2</sub> -Polyaniline [112]	Heterostructure thin film	25	50 ppb	5%	5 min	15 min	0.33
RGO/poly(3,4-ethylenedioxythiophene) [113]	Nanocomposite	RT	1	0.05	<180	<70	0.0003
Pd-SnO <sub>2</sub> -RGO [68]	Nanosheets	RT	1	3.92	13	105	0.30
RGO/Au [71]	Nanocomposite	50	5	1.33	132	386	0.002
Mixed p-Type MoS <sub>2</sub> [76]	Flakes	RT+UV	10	21.78	6.09	146.49	0.36
MoS <sub>2</sub> [77]	Nanowire networks	60	5	18.1	16	172	0.23
Nb doped-MoSe <sub>2</sub> [78]	2D Layered	150	3	8.03	<30	-	0.09
PS/WO <sub>3</sub> -Pd60 [84]	Nanorods	RT	2	5.2	10	339	0.26
Polycrystalline PdO [85]	Ultrathin films	175	10	1.63	<500	600–700	0.0003
ZnO [86]	Nanorods	200	100	622	35	206	0.177
ZnO [86]	Bunch of nanowires	200	100	101	17	290	0.06
Microwave-Synthesized NiO [87]	Film	25	3	4991	30	45	55.4
On-chip grown Zn <sub>2</sub> SnO <sub>4</sub> [89]	Nanowires	200	10	35	<100	<150	0.035
BGaN/GaN superlattice [94]	Double Schottky junction	250	450	31	5	80	0.013
Pt-AlGaN/GaN [95]	HEMT	300	900	33	27 min	-	2.2 × 10 <sup>-5</sup>
		600	900	38.5	1.2 min	-	0.0006
SnO <sub>2</sub> -AlGaN/GaN [96]	Heterostructure	250	500 ppb	13%	165	280	0.16
PCDTBT [98]	OFET	RT	10	160	6.5 min	33 min	0.041
Copper Phthalocyanine (CuPc) [100]	Thin film transistor	RT	20	>550	-	>3 days	negligible
MoS <sub>2</sub> -RGO [102]	Nanosheets	160	3	1.23	8	20	0.05
ZnO/poly(3-hexylthiophene) [103]	Nanosheet-nanorod	RT	4	59	<15 min	<45 min	0.02

### 3. Recent Advances in SO<sub>2</sub> Gas Detection

#### 3.1. Carbon Material-Based SO<sub>2</sub> Sensors

Aligned carbon nanotubes possess high surface-to-volume ratios which promote efficient physical and chemical adsorption of target gases [114]. Recently Zouaghi et al. have initiated research on vertically aligned carbon nanotube (VACNT)-based gas sensors interrogated by THz radiation [115]. They synthesized VACNT on SiO<sub>2</sub> coated, boron-doped Si substrate by a water-assisted chemical vapor deposition method. Figure 7A shows a SEM image of vertically aligned CNT indicating a layer thickness of 95 μm. The transmission spectrum upon SO<sub>2</sub> gas exposure is illustrated in Figure 7B. The denser rotational spectrum of SO<sub>2</sub> is attributed to the bent structure of SO<sub>2</sub> molecule. The highest relative transmittance was obtained around 0.2 THz. When SO<sub>2</sub> gas was flowed abruptly into a Si/SiO<sub>2</sub>/VACNT sensor, the maximum of transmitted electric field amplitude decreased to a steady value with fast response time of 2–3 min (Figure 7C). However, the recovery time was too long (>70 min). It has been predicted that the slow recovery was caused from the high sticking coefficient of SO<sub>2</sub> gas to steel walls in the system. In a previous research, cholesteric-nematic mixture intercalated with CNT walls had been prepared and physical adsorption between the CNT and SO<sub>2</sub> molecules was observed [116]. This adsorption phenomenon altered the CNT conductivity that in turn resulted into sensing signal for SO<sub>2</sub>. Zhang et al. synthesized TiO<sub>2</sub>/graphene film using layer-by-layer self-assembly technique for room temperature SO<sub>2</sub> detection [117]. Excellent contacts between TiO<sub>2</sub> and rGO are achieved from the wrapping of rGO flakes on TiO<sub>2</sub> nanosphere surface or bridge-connection between TiO<sub>2</sub> balls as shown in SEM image (Figure 7D). The sensor was exposed to 1, 50, 250, 1000 ppb SO<sub>2</sub> gas to study the response-recovery behavior plotted in Figure 7E. It was observed that with increasing gas concentration, the sensor response kept increasing but the response-recovery time became longer. It has been predicted that the large interspace is responsible for the increase of response and recovery time. The TiO<sub>2</sub>/rGO film sensor showed much higher sensitivity to 1 ppm SO<sub>2</sub> gas at room temperature than other target gases such as—CH<sub>4</sub>, C<sub>2</sub>H<sub>2</sub>, H<sub>2</sub>, CO, NO<sub>2</sub> (Figure 7F). So, the synthesized sensor was selective enough to SO<sub>2</sub> gas.

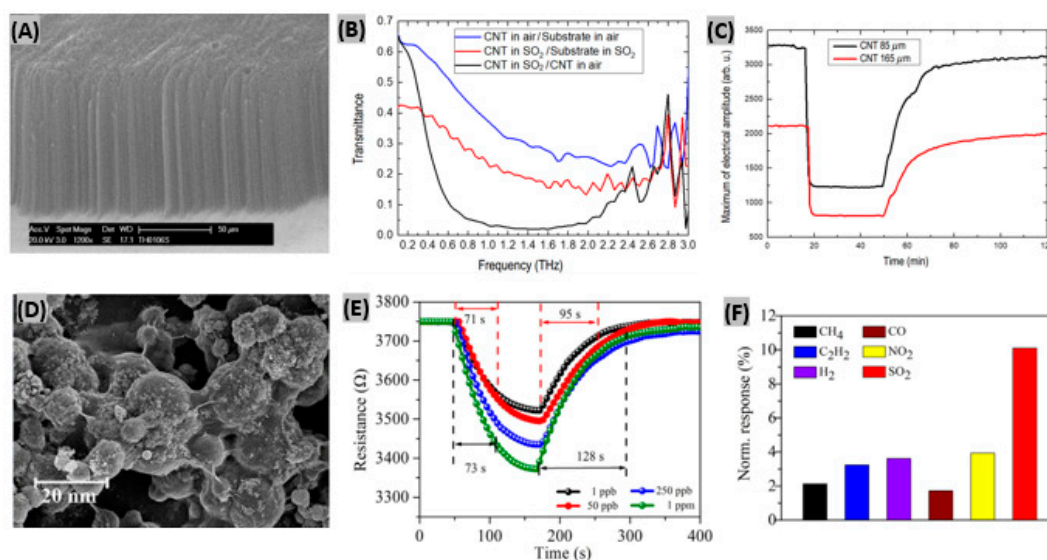


**Figure 7.** (A) SEM image of a VACNT layer on Si/SiO<sub>2</sub> substrate. (B) Normalized transmittance spectra of Si/SiO<sub>2</sub>/VACNT in air and SO<sub>2</sub>. (C) Maximum of electrical amplitude vs. time response in transmission measurements with 85 μm and 165 μm thick layers of VACNT. Figures adapted with permission from [114], Copyright 2018 Lietuvos mokslų akademija. (D) SEM image of self-assembled TiO<sub>2</sub>/rGO film. (E) Response/recovery curves of TiO<sub>2</sub>/rGO sensor exposed to four different concentrations of SO<sub>2</sub> gas. (F) Normalized response of TiO<sub>2</sub>/rGO sensor toward 1 ppm of various gases at room temperature. Figures adapted with permission from [116], Copyright 2017 Elsevier.

### 3.2. Metal and Metal-Oxide Nanostructures-Based SO<sub>2</sub> Sensors

Many attempts had been made for SO<sub>2</sub> gas detection using various semi-conducting metal oxides, such as- CeO<sub>2</sub>, WO<sub>3</sub>, V<sub>2</sub>O<sub>5</sub>-TiO<sub>2</sub>, MoO<sub>3</sub>-SnO<sub>2</sub> and NiO [118]. However, due to instability in the highly reducing atmospheres, these sensors can only operate at low temperature (<500 °C) [119]. Liu et al. fabricated ZnO nanosheets decorated with Ru/Al<sub>2</sub>O<sub>3</sub> catalyst and integrated them with a microsensor to detect SO<sub>2</sub> gas [120]. Inkjet printing technology was used to load the sensor. AFM image in Figure 8A reveals the uniformity of the prepared ZnO 2D nanosheet and the thickness is indicated as about 1.5 nm. Different concentrations of SO<sub>2</sub> gas had been exposed to Ru/Al<sub>2</sub>O<sub>3</sub>/ZnO sensor and the corresponding resistance responses are shown in Figure 8B. It is seen that resistance notably decreased at SO<sub>2</sub> exposure and percent sensor response increased linearly with SO<sub>2</sub> concentration. At 25 ppm of SO<sub>2</sub>, the obtained response and recovery times were about 1 min and 6 min, respectively. The SO<sub>2</sub> selectivity test is displayed in Figure 8C, where the fabricated sensor responded negligibly to the test gases CO, CH<sub>3</sub>OH, C<sub>2</sub>H<sub>5</sub>OH, acetone, CO<sub>2</sub>, NO and HCHO in comparison to SO<sub>2</sub> gas. From on-line mass spectrometry experiments, it was found that the catalyst Ru/Al<sub>2</sub>O<sub>3</sub> dissociates SO<sub>2</sub> molecules into easily detectable SO• species. Being captured by ZnO nanosheet, these species contribute to the sensor output signal. In another study, Ciftyürek et al. prepared and then evaluated molybdenum and tungsten binary and ternary oxide thick films for gas sulfur species sensing [121]. It was found that hydrothermally synthesized nano-SrMoO<sub>4</sub> exhibited the highest sensor response among those fabricated oxide films. The SrMoO<sub>4</sub>-based sensors were able to operate at very high temperature (>600 °C) while maintaining their sensing performances, and thus can be useful in gas monitoring at industries. SnO<sub>2</sub> thin film had been prepared by Tyagi et al. [122] using sputtering technique. Then, the film was functionalized with various metal oxide catalyst such as- PdO, CuO, NiO, MgO, V<sub>2</sub>O<sub>5</sub> to make SO<sub>2</sub> gas sensor. The uniform distribution of NiO nanoclusters on the surface of SnO<sub>2</sub> film is noticed in the SEM image (Figure 8D). 500 ppm of SO<sub>2</sub> gas was exposed to different metal-oxides deposited on SnO<sub>2</sub> sensors to study the response at various operating temperatures (Figure 8E). NiO/SnO<sub>2</sub> structure showed the highest response (~56) at 180 °C due to two main reasons. Firstly, the spill-over effect from NiO nanoclusters toward SO<sub>2</sub> molecules. Secondly, increase of adsorbed oxygen species sites at the porous and rough surface of SnO<sub>2</sub> film [123]. The response and recovery time of NiO/SnO<sub>2</sub> sensor were estimated as 80 s and 70 s respectively towards 500 ppm of SO<sub>2</sub> gas at 180 °C as shown in Figure 8F. Also, the sensor exhibited good reproducibility and selectivity under SO<sub>2</sub> exposure. In another study, it had been reported that BiFeO<sub>3</sub> is highly selective to SO<sub>2</sub> against carbon monoxide and butane [124]. Also, it was found that BiFeO<sub>3</sub> synthesized by a sonochemical method provides better sensing performances than when prepared by conventional methods.

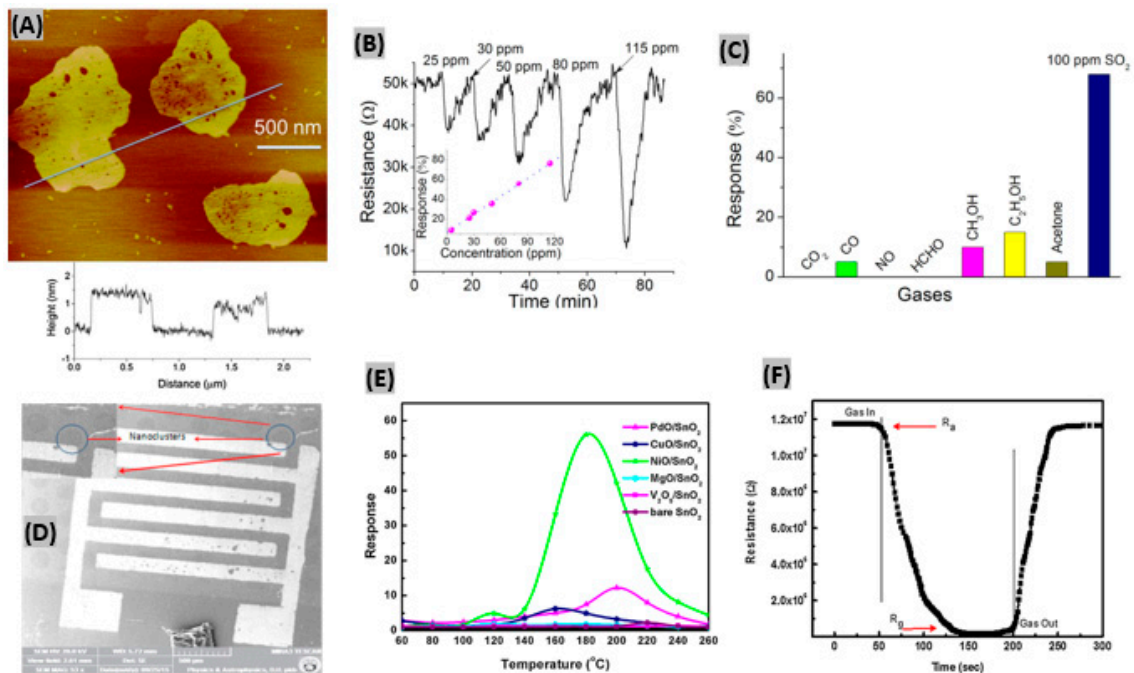


**Figure 8.** (A) Two-dimensional AFM image of ZnO nanosheets, height profile of two ZnO nanosheets as marked is shown below. (B) Resistance changes to SO<sub>2</sub> gas at different concentrations, inset shows plotting of sensing response vs. SO<sub>2</sub> concentration (C) Selectivity test of Ru/Al<sub>2</sub>O<sub>3</sub>/ZnO sensor to various gases under same concentration. Figures adapted with permission from [119], Copyright 2018 Elsevier. (D) SEM image of NiO/SnO<sub>2</sub> sensor structure, inset displays the presence of NiO nanoclusters. (E) Sensor response of NiO/SnO<sub>2</sub>, PdO/SnO<sub>2</sub>, CuO/SnO<sub>2</sub>, MgO/SnO<sub>2</sub>, V<sub>2</sub>O<sub>5</sub>/SnO<sub>2</sub> and bare SnO<sub>2</sub> structures with operating temperatures towards 500 ppm of SO<sub>2</sub> gas. (F) SO<sub>2</sub> gas response-recovery illustration for NiO/SnO<sub>2</sub> sensor. Figures adapted with permission from [121], Copyright 2015 Elsevier.

### 3.3. GaN-Based SO<sub>2</sub> Sensors

AlGaN/GaN heterostructure semiconductors facilitate low power consumption, miniaturization and excellent sensing performances [125]. Also, AlGaN/GaN-based sensors can operate in chemically harsh environments, at high temperatures and under radiation fluxes due to having thermally and chemically stable structures [126]. Triet et al. synthesized Al<sub>0.27</sub>Ga<sub>0.73</sub>N/GaN-based Schottky diode sensors for SO<sub>2</sub> gas detection [127]. Vertical zinc oxide nanorods (ZnO NRs) and a RGO nanosheet hybrid was formed on a AlGaN/GaN/sapphire heterostructure where the RGO and AlGaN surface made a Schottky contact with each other. From the FE-SEM image in Figure 9A, it is observed that neighboring ZnO NRs are attached to each other by RGO. During the gas exposure, the Schottky barrier between RGO and AlGaN layers changes. As a result, thermionic emission carrier transport is altered which in turn modifies the reverse saturation current. In the case of detecting SO<sub>2</sub> (Figure 9B), the resistance response increased with increasing gas concentration because SO<sub>2</sub> molecules are electron withdrawers. The non-linearity of the response with gas concentration is attributed to incomplete recovery of the sensing material RGO-ZnO NRs (Figure 9C). Here, SO<sub>2</sub> gas molecules react with interaction sites resulting into slow diffusion of gas molecules within the RGO multilayer structure [128].

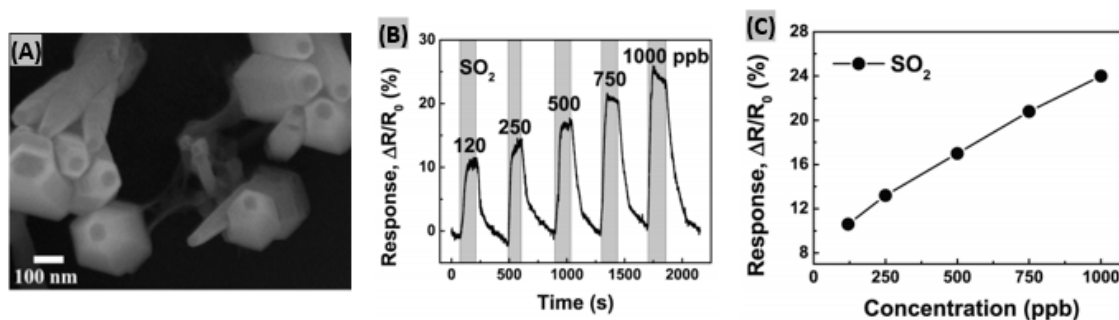


**Figure 9.** (A) Top-view of FE-SEM high magnification image of the RGO nanosheets connecting to ZnO NRs on AlGaIn/GaN heterostructure. (B) Sensor resistance variations at the exposure to  $\text{SO}_2$  gas of different concentrations. (C) Response vs. gas concentration relationship under  $\text{SO}_2$  gas exposure. Figures adapted with permission from [126], Copyright 2017 American Chemical Society.

### 3.4. Solid Electrolyte-Based $\text{SO}_2$ Sensors

Different solid electrolytes such as- NASICON [129], YSZ [130] and alkali metal sulfates [131] have been exploited during the past decades to fabricate high performance  $\text{SO}_2$  sensors. Among all the solid electrolytes, NASICON is widely used in the mixed-potential sensors due to its high ionic conductivity. Ma et al. [132] reported a mixed-potential gas sensor using NASICON and orthoferrite ( $\text{La}_{0.5}\text{Sm}_{0.5}\text{FeO}_3$ ) as sensing electrode. The SEM image of powdered  $\text{La}_{0.5}\text{Sm}_{0.5}\text{FeO}_3$  having a perovskite crystal structure reveals the uniformity of size and porosity (Figure 10A).  $\text{La}^{3+}$  doping level had been varied to study the variation of sensing performances. The highest response ( $-86.5$  mV) was obtained for sensor with  $\text{La}_{0.5}\text{Sm}_{0.5}\text{FeO}_3$  as sensing electrode to 1 ppm  $\text{SO}_2$  (Figure 10B). The response order was found as  $\Delta V(\text{La}_{0.5}) > \Delta V(\text{La}_{0.4}) > \Delta V(\text{La}_{0.6}) > \Delta V(\text{La}_{0.8}) > \Delta V(\text{La}_{0.2})$ . The porous structure and electrocatalytic property are possibly responsible for the variation of responses. Responses were recorded at different operating temperatures. The equity between the amount of adhering gas and the activation energy demand indicated  $275$  °C as the optimum operating temperature with the highest response. The prepared mixed-potential sensor was exposed to other test gases such as-  $\text{NO}_2$ ,  $\text{Cl}_2$ ,  $\text{NH}_3$ ,  $\text{CO}$ ,  $\text{NO}$ , acetone,  $\text{H}_2$ ,  $\text{CH}_4$ , ethanol and methanol for a gas selectivity test. The sensor remained selective enough to detect  $\text{SO}_2$  gas even in very low amounts as illustrated in Figure 10C. In another study, a zirconia-based solid state electrochemical  $\text{SO}_2$  sensor had been demonstrated with  $\text{MnNb}_2\text{O}_6$  as sensing electrode [133]. Under very high operating temperature ( $700$  °C), the sensor attained good sensitivity along with rapid and stable response-recovery of gas molecules.

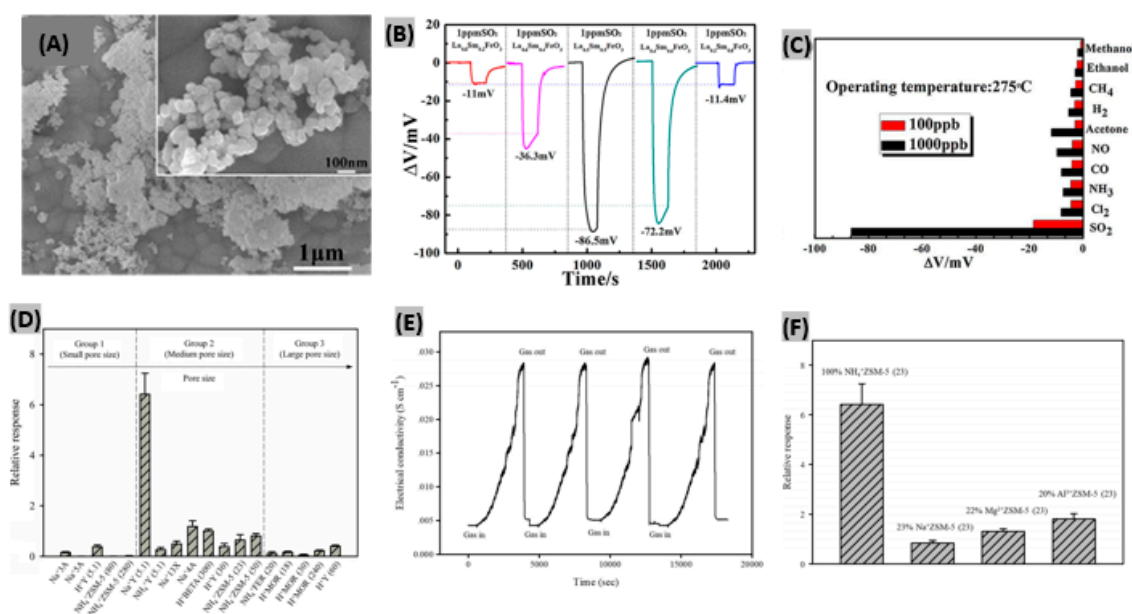


**Figure 10.** (A) SEM image of powdered  $\text{La}_{0.5}\text{Sm}_{0.5}\text{FeO}_3$ , inset shows higher magnified image. (B) The voltage change response of the gas sensor made with  $\text{La}_x\text{Sm}_{1-x}\text{FeO}_3$  sensing electrodes ( $x = 0.2, 0.4, 0.5, 0.6, 0.8$ ). (C) The selectivity test for the sensor using  $\text{La}_{0.5}\text{Sm}_{0.5}\text{FeO}_3$  as sensing electrode to various gases at 275 °C. Figures adapted with permission from [131], Copyright 2017 Elsevier. (D) Comparative responses of different pristine zeolites. (E) Sensor response of  $\text{NH}_4^+\text{ZSM-5}$  (23) exposed to 4200 ppm  $\text{SO}_2$  for four cycles. (F) Comparative responses of different ion-exchanged ZSM-5 (23) zeolite sensors. Figures adapted with permission from [134], Copyright 2018 Springer-Verlag GmbH Germany, part of Springer Nature.

### 3.5. Zeolite-Based $\text{SO}_2$ Sensors

Zeolites are aluminosilicates possessing immensely porous crystal structure, high specific surface area, high chemical and thermal stability, good adsorption properties, alterable chemical composition, presence of mobile ions, ability to undergo ion-exchange process and variable hydrophobic or hydrophilic features [134,135]. These characteristics make zeolites very attractive for gas detection. Choeichom et al. studied the effects of zeolite type, cation type and Si/Al ratio within various zeolites when exposed to  $\text{SO}_2$  gas [136]. During the exposure to 4200 ppm  $\text{SO}_2$ , pristine zeolites exhibited the different sensor responses plotted in Figure 10D. It was found that the relative response of each pristine zeolite type showed the following decreasing order: ZSM-5 > beta > 13X > Y > 4A > ferrierite > mordenite > 5A > 3A. The three key factors contributing to the variation of these zeolite responses are pore size, cation type and Si/Al ratio. It was observed that the relative response increases with increasing zeolite pore size, however, decreases with a too large pore size. Among the monovalent cation zeolites focused here, the  $\text{NH}_4^+$  zeolite response was the highest because of formation of hydrogen bonds with more than one  $\text{SO}_2$  molecule. With decreasing of Si/Al ratio, the responses kept increasing. The combined effect of the above discussed factors contributed to  $\text{NH}_4^+\text{ZSM-5}$  (23) achieving the highest relative response toward  $\text{SO}_2$  with 23 as Si/Al ratio and medium pore size. Recovery and repeatability assessments were performed by flowing 4200 ppm  $\text{SO}_2$  for four cycles as illustrated in Figure 10E. The sensor conductivity returned to its initial value after  $\text{SO}_2$  was removed and again produced the same response to  $\text{SO}_2$  in the subsequent cycles. These results indicate the complete recovery and strong repeatability of the zeolite sensor. The sensor responses of various ion-exchanged ZSM-5 (23) towards 4200 ppm  $\text{SO}_2$  had been investigated as well (Figure 10F). It was found that  $\text{Al}^{3+}\text{ZSM-5}$  (23) provides the highest relative response due to two key factors: firstly, the magnitude of the ion-dipole attraction increases with the increasing ionic charge.  $\text{Al}^{3+}$  having higher ionic charge than  $\text{Mg}^{2+}$  and  $\text{Na}^+$ , promotes a higher degree of interaction with  $\text{SO}_2$  molecules

which in turn results in a higher sensor response. Secondly, the higher electronegativity of  $\text{Al}^{3+}$ ZSM-5 (23) governs the stronger cation-dipole interaction with  $\text{SO}_2$  and thus facilitates a higher sensor response. Recently, a zinc-doped zeolitic imidazolate framework (ZIF-67) attached with CNT has been reported as  $\text{SO}_2$  sensing material [137]. It provided notable sensing performances at room temperature due to its porous polyhedral structure of metal particles with numerous interlinked CNTs. Previously, conductive polymer/zeolite composite based  $\text{SO}_2$  detection had been studied [138]. It was observed that PEDOT-PSS/KY zeolite composite achieved the highest sensor response having gas adsorption–desorption dependence on the cation types of Y zeolite.

### 3.6. Paper-Based $\text{SO}_2$ Sensors

Sensing materials incorporated onto paper offer color transition sensing with the eyes, whereby measurement systems and electric circuits are not needed [139]. Paper-based analytical devices (PADs) provide the advantages of ease of production, low cost, flexibility, efficient sample collection, and easy disposability [140]. Li et al. coupled headspace sampling (HS) with PAD in order to detect  $\text{SO}_2$  through surface-enhanced Raman scattering (SERS) [141]. Hybrids consisting of 4-mercapto-pyridine (Mpy)-modified gold nanorods (GNRs) and reduced graphene oxide (rGO) were prepared. Then along with anhydrous methanol and starch iodine complex, the rGO/MPy-GNRs hybrids were immobilized upon cellulose-based filter papers using a vacuum filtration method. This process promotes the formation of a dense blue colored film on the filter paper as shown in the SEM images (Figure 11A–C). Uniform cellulose fibers of  $12.5\ \mu\text{m}$  width adopt wrinkle-like structures because of the attachment with rGO (Figure 11B). On exposing the fabricated rGO/MPy-GNRs/SIC paper to  $\text{SO}_2$ , the blue color faded within minutes as illustrated in Figure 11C. It was found that the intermolecular charge-transfer complex between starch and iodine produces a broad band at 600 nm as indicated by curve d of Figure 11D.

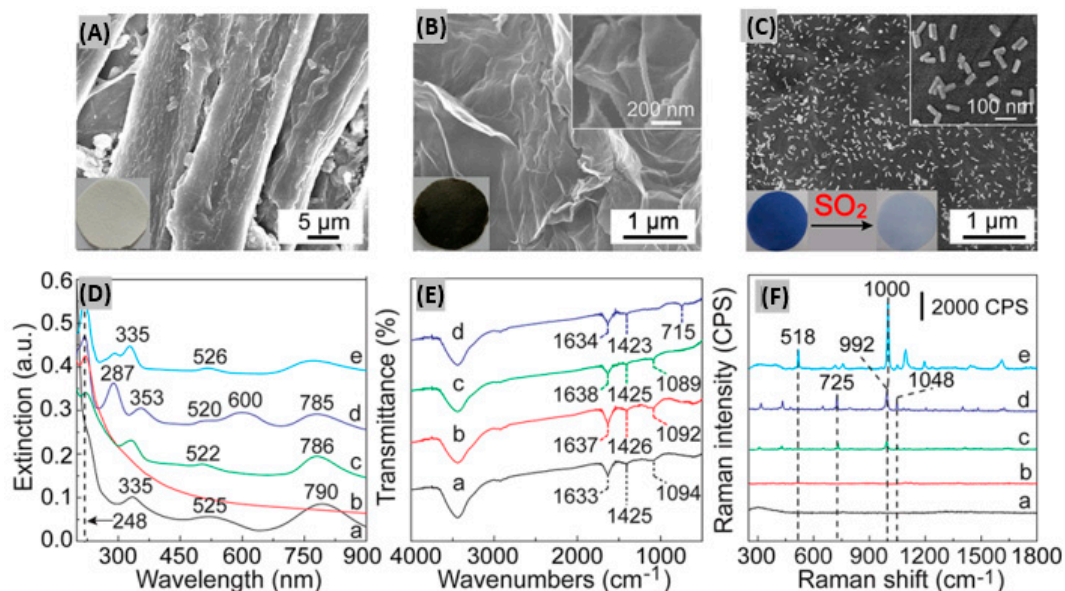


**Figure 11.** SEM images of (A) pure cellulose paper, (B) after assembling with rGO and (C) rGO/MPy-GNRs/SIC paper. Insets of figures (A–C) show pictures of the corresponding paper substrate under light. (D) UV-vis-NIR extinction spectra of (a) MPy-GNRs paper, (b) rGO paper, (c) rGO/MPy-GNRs paper, rGO/MPy-GNRs/SIC paper (d) before and (e) after the adsorption of  $\text{SO}_2$ , respectively. (E) FT-IR spectra of (a) MPy-GNRs, (b) rGO/MPy-GNRs, rGO/MPy-GNRs/SIC (c) before and (d) after the adsorption of  $\text{SO}_2$ , respectively. (F) SERS spectra of (a) the pure cellulose paper, (b) the rGO paper, (c) the MPy-GNRs paper, rGO/MPy-GNRs/SIC paper (d) before and (e) after adsorption of  $\text{SO}_2$ , respectively. Figures adapted with permission from [140], Copyright 2018 American Chemical Society.

The IR spectrum of rGO/MPy-GNRs/SIC is displayed in Figure 11E indicating the modification in the response after SO<sub>2</sub> exposure. Along with the distinct and typical peaks for MPy, SO<sub>2</sub> adsorption introduces a new peak having increased intensity in the SERS spectra of rGO/MPy-GNRs/SIC as shown by curve e in Figure 11F. This additional peak occurs because SO<sub>2</sub> possibly affects the bending vibration of pyridine, and the characteristic peaks of SO<sub>2</sub>-pyridine complex are reflected in the bands. Recently, an amino-functionalized luminescent MOF material (MOF-5-NH<sub>2</sub>) was incorporated onto test paper for portable SO<sub>2</sub> sensing [142]. It was seen that the prepared luminescent paper got lightened upon SO<sub>2</sub> gas exposure with high selectivity. Also, it detected as low as 0.05 ppm SO<sub>2</sub> having reusability advantages. In another research work, a microfluidic paper-based integrated detection system had been reported to monitor SO<sub>2</sub> concentrations using RGB color analysis software [143]. The sensing performance metrics like sensitivity/response, response and recovery times at certain gas concentration and operating temperatures, and sensitivity per ppm/response time ratio for different SO<sub>2</sub> sensor materials and structures have been summarized in Table 2. It provides a brief comparative performances outline among different SO<sub>2</sub> sensor reported in recent years.

**Table 2.** Gas sensing properties of recently developed SO<sub>2</sub> gas sensors.

Materials	Structure	Operating Temperature (°C)	Concentration (ppm)	Sensitivity/Response	Response Time (s)	Recovery Time (s)	Sensitivity per ppm Response time
Polyaniline [144]	Nanoneedles	RT	10	4.2	180	<180	0.0023
Polyaniline-WO <sub>3</sub> [145]	Nanocomposite	RT	10	10.6	180	180	0.006
SnO <sub>2</sub> [146]	Thin films	RT	1	138	-	-	-
Au/ZnO [147]	Thin films	RT	10	1.1	20 min	50 min	0.0001
Li <sub>3</sub> PO <sub>4</sub> -Li <sub>2</sub> SO <sub>4</sub> /V <sub>2</sub> O <sub>5</sub> [148]	Electrolyte film	500	10	30	5 min	10 min	0.01
SnO <sub>2</sub> -TiO <sub>2</sub> [149]	Composite (75 mol% of TiO <sub>2</sub> )	450	10	55	5 min	>5 min	0.02
g-C <sub>3</sub> N <sub>4</sub> /rGO [150]	2D stacking hybrid	RT	20	0.01 ppm <sup>-1</sup>	204	276	0.5 × 10 <sup>-4</sup>
g-C <sub>3</sub> N <sub>4</sub> /rGO [150]	2D stacking hybrid	RT + UV	2	0.0032 ppm <sup>-1</sup>	140	130	2.3 × 10 <sup>-5</sup>
Polyaniline [151]	Porous nanofibers	RT	5	4.5%	185	<200	0.005
Au-PANI [112]	Heterostructured thin film	RT	2	300	-	-	-
TiO <sub>2</sub> /rGO [116]	Nanocomposite	RT	1	10.08	73	128	0.14
Ru/Al <sub>2</sub> O <sub>3</sub> /ZnO [119]	Nanosheets	350	25	20	60	6 min	0.013
SrMoO <sub>4</sub> [120]	nanoflowers	600	2000	-17.2	15.6 min	<30 min	1 × 10 <sup>-5</sup>
NiO/SnO <sub>2</sub> [121]	Thin film	180	500	56	80	70	0.0015
RGO-ZnO on 2DEG AlGaIn/GaN [125]	Nanorods	RT	120 ppb	14	120	320	0.98
NASICON-La <sub>0.5</sub> Sm <sub>0.5</sub> FeO <sub>3</sub> [130]	Thick film electrolyte	275	1	86.5	44	100	1.96
Zirconia-MnNb <sub>2</sub> O <sub>6</sub> [131]	Electrolyte-electrode	700	5	27	10	>10	0.54
NH <sub>4</sub> <sup>+</sup> ZSM-5 (23) [134]	Zeolites and molecular sieves	RT	4200	6.41	63 min	3 min	0.4 × 10 <sup>-6</sup>
CoZn-NCNTs [136]	Nanotube	RT	0.5	8.45%	32	900	0.53
PEDOT-PSS/Y zeolite [137]	Polymer/zeolite composite	27	1000	5	>9.4 min	Longer	0.8 × 10 <sup>-5</sup>
MOF-5-NH <sub>2</sub> [141]	Luminescent probe	RT	0.168	1000 (luminescence intensity, au)	<15	-	396

## 4. Recent Advances in H<sub>2</sub>S Gas Detection

### 4.1. Carbon Material-Based H<sub>2</sub>S Sensors

In recent years, many research efforts have been made for H<sub>2</sub>S detection using graphene, reduced graphene oxide and carbon nanofibers. Ovsianyt'skyi et al. [152] proposed a graphene-based H<sub>2</sub>S gas sensor functionalized with Ag nanoparticles (Ag NPs) and charged impurities. Graphene was grown by the CVD technique, and then Ag NPs and impurities were incorporated on the graphene by a wet chemical method. The SEM image of graphene after immersing into AgNO<sub>3</sub>/Fe(NO<sub>3</sub>)<sub>3</sub> solution reveals the presence of large number of nanoparticles (10–100 nm) uniformly distributed on its surface (Figure 12A). The comparative responses obtained on exposing 500 ppb of H<sub>2</sub>S gas for 400 s to pristine graphene, graphene doped with Fe(NO<sub>3</sub>)<sub>3</sub> solution, graphene doped with AgNO<sub>3</sub> solution, and graphene doped with a mixed AgNO<sub>3</sub>/Fe(NO<sub>3</sub>)<sub>3</sub> solution are displayed in Figure 12B. Graphene doped with the mixed solution exhibited the highest response. Since Ag is less electronegative than graphene, adsorption of H<sub>2</sub>S occurs because of its interaction with the adsorbed oxygen species on Ag mostly. Then, electrons released from dissociation of H<sub>2</sub>S are accumulated in graphene. This phenomenon causes a decrease in graphene hole concentration, and thus resistance of Ag-doped graphene increases.

The relationship between gas concentrations and corresponding relative responses of the synthesized sensor is quite linear, as plotted in Figure 12C. Also, the sensor was strongly selective to H<sub>2</sub>S gas against CH<sub>4</sub>, CO<sub>2</sub>, N<sub>2</sub>, and O<sub>2</sub> gases. Similarly, Chu et al. [153] obtained a sensitivity of 34.31% toward 100 ppm H<sub>2</sub>S with tin oxide-modified reduced graphene oxide (SnO<sub>2</sub>-rGO) at 125 °C. In another study, Zhang et al. [154] developed a stable sensor using ZnO-carbon nanofibers (30.34 wt% carbon) that exhibited good H<sub>2</sub>S sensing performances. It was found that the protection of carbon provides high stability of ZnO and oxygen vacancies to allow improved sensor responses.

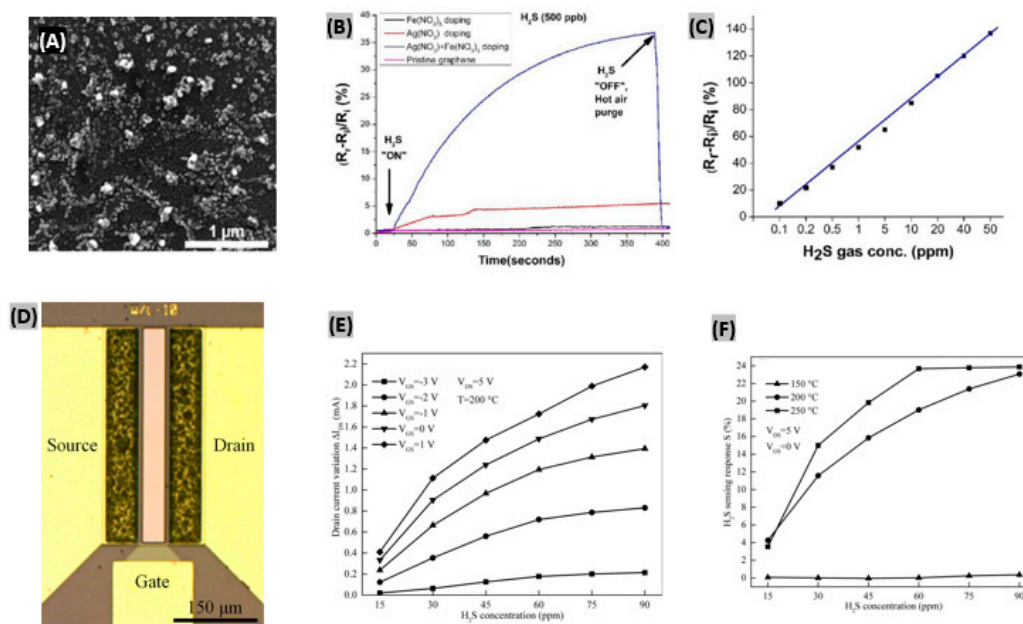


**Figure 12.** (A) SEM image of graphene after immersion into AgNO<sub>3</sub>/Fe(NO<sub>3</sub>)<sub>3</sub> solution. (B) Comparative sensor responses of pristine graphene, graphene doped with Fe(NO<sub>3</sub>)<sub>3</sub> solution, graphene doped with AgNO<sub>3</sub> solution, and graphene doped with mixed Fe(NO<sub>3</sub>)<sub>3</sub> and AgNO<sub>3</sub> solution. (C) Relationship between H<sub>2</sub>S gas concentrations and corresponding relative responses of the fabricated sensor. Figures adapted with permission from [152], Copyright 2017 Elsevier. (D) Top view of the optical micrograph of the fabricated Pt-AlGaIn/GaN HEMT sensor. (E) Changes in drain current with different concentrations of H<sub>2</sub>S gas and gate biases at T = 200 °C, V<sub>DS</sub> = 5 V. (F) Sensitivity of the fabricated sensor toward H<sub>2</sub>S at different temperatures. Figures adapted with permission from [155], Copyright 2018 Elsevier.

## 4.2. GaN-Based H<sub>2</sub>S Sensors

Several AlGaN/GaN-based gas sensors have been reported, including NO, NO<sub>2</sub>, NH<sub>3</sub>, Cl<sub>2</sub>, CO, CO<sub>2</sub> and CH<sub>4</sub> [156–158]. However, H<sub>2</sub>S sensing using wide bandgap semiconductors like GaN have not been explored yet that much. In order to sense H<sub>2</sub>S gas even at very low amounts, Sokolovskij et al. [155] synthesized AlGaN/GaN HEMT-based sensor with platinum as gate. The top view optical micrograph of the synthesized device shown in Figure 12D reveals the gate dimensions, gate-source and gate-drain spacing. For high temperature operations, each device was wire bonded to ceramic substrates. The variation of drain current was observed under different H<sub>2</sub>S concentrations and gate bias voltages (Figure 12E).

Because of the increasing baseline current with increasing gate bias, variation of the drain current was highly influenced. Also, the fabricated HEMT sensor operates in a wide range of biasing conditions without degrading the sensing performances and thus shows an excellent stability. It was found that when gate bias approaches pinch-off state, it minimizes power consumption and thus enables the sensor to operate at high response mode. The sensitivity of AlGaN/GaN HEMT sensor clearly increases with higher temperatures as plotted in Figure 12F. The rise and fall time were estimated 219 s and 507 s, respectively, at 250 °C. At lower temperatures, rise and fall times have gone higher. Further, Zhang et al. [159] pre-treated the Pt-gated AlGaN/GaN HEMT sensor with H<sub>2</sub> pulses in dry air ambient at 250 °C. This treatment facilitated the enlargement of the H<sub>2</sub>S detection range up to 90 ppm.

## 4.3. Metal and Metal Oxide-Based H<sub>2</sub>S Sensors

### 4.3.1. Nanostructured Metal Oxide-Based Sensors

It was found that metal oxides such as- SnO<sub>2</sub>, WO<sub>3</sub>, ZnO, and  $\alpha$ -Fe<sub>2</sub>O<sub>3</sub> based sensors exhibited superior sensing performances toward H<sub>2</sub>S due to their stable nanostructures [160–162]. Zhang et al. [163] reported a  $\alpha$ -Fe<sub>2</sub>O<sub>3</sub> nanosheet-based H<sub>2</sub>S gas sensor using a solvothermal method. Figure 13A shows the SEM image of a sample obtained at reaction temperature of 160 °C denoted as S<sub>160</sub>. It was observed that at low temperatures, the morphology of the samples is not uniform. Since both  $\alpha$ -Fe<sub>2</sub>O<sub>3</sub> and Fe<sub>3</sub>O<sub>4</sub> exist in the nanostructure, uniform morphology can't be obtained under the reaction temperature of 160 °C. It was seen that sensor response of  $\alpha$ -Fe<sub>2</sub>O<sub>3</sub> to H<sub>2</sub>S decreases with the increasing working temperature. However, the recovery time is too long at low temperature, so taking sensor response, response time and recovery time into account, 135 °C was estimated as the optimum working temperature. Figure 13B displays the response of the prepared sensor to different concentrations of H<sub>2</sub>S ranging from 1 to 50 ppm at 135 °C. The response and recovery time were estimated to be less than 10 s and 45 s, respectively, indicating very a rapid response in comparison to other H<sub>2</sub>S gas sensors. The changes in the electric resistances were found negligible for the sensor to 50 ppm acetone, ethanol, methanol and H<sub>2</sub> gases at 135 °C. On the contrary, the sensor response was very large to H<sub>2</sub>S under same conditions, thus reflecting excellent selectivity of the  $\alpha$ -Fe<sub>2</sub>O<sub>3</sub> nanosheet-based H<sub>2</sub>S sensor (Figure 13C).

In another study, Li et al. [164] developed ZnO/CuO nanotube arrays to sense H<sub>2</sub>S at low-working temperatures. It was observed that the nanotube structures promoted the diffusion and adsorption of gas with many active sites between H<sub>2</sub>S molecules and adsorbed oxygen molecules. Thus, they contributed to achieve good sensitivity along with fast response time. It was found that porous In<sub>2</sub>O<sub>3</sub> nanoparticles provide large surface areas and pore volumes which create numerous active sites to produce active oxygen species [165]. These sites facilitate a significant improvement in H<sub>2</sub>S gas sensing with 1 ppb of detection limit. Also, a dense array of intrinsic ZnO NWs has been reported for H<sub>2</sub>S detection by exploiting a sulfuration–desulfuration reaction mechanism [166]. In another work, Eom et al. [167] fabricated Cu<sub>x</sub>(x=1,2)O:SnO<sub>2</sub> thin films to detect H<sub>2</sub>S gas at room temperature. Enhanced sensitivity with rapid response-recovery was obtained due to enhanced adsorption sites arising from abounding domains of p-n heterojunctions on the Cu<sub>x</sub>O:SnO<sub>2</sub> film surfaces. Besides, a Cu-doped BaSrTiO<sub>3</sub>-based H<sub>2</sub>S sensor was reported [168]. Herein along with gas-surface interaction,

the role of pre-adsorbed oxygen species and surface dipolar hydroxyl groups has been investigated as well.

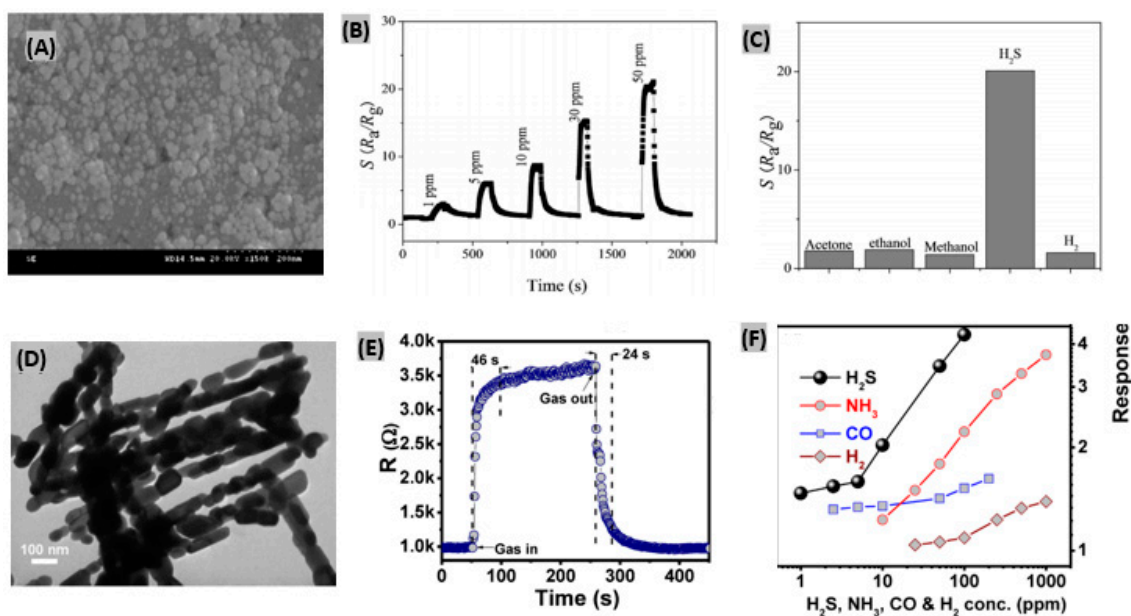


**Figure 13.** (A) SEM image of  $\alpha\text{-Fe}_2\text{O}_3$  nanosheets sample obtained at reaction temperature of 160 °C denoted as  $S_{160}$ . (B) Sensor responses of  $\alpha\text{-Fe}_2\text{O}_3$  nanosheets to various  $\text{H}_2\text{S}$  concentrations at 135 °C. (C) Sensor responses of the synthesized sensor to 50 ppm of various gases at 135 °C. Figures adapted with permission from [163], Copyright 2018 Elsevier. (D) TEM image of the fabricated mesoporous  $\text{Co}_3\text{O}_4$  nanochains. (E) Sensor response–recovery curve at 100 ppm of  $\text{H}_2\text{S}$  gas at 300 °C. (F) Sensing response of the prepared  $\text{Co}_3\text{O}_4$  sensor to various gases at 300 °C. Figures adapted with permission from [169], Copyright 2018 Elsevier.

#### 4.3.2. Mesoporous Metal Oxide-Based Sensors

Generally mesoporous materials contain pores with diameters of 2–50 nm. Mesoporous metal-oxides offer efficient gas detection because they have large surface areas, open porosity, small pore sizes, and the ability to coat the surface of the mesoporous structure with one or more compounds. Quang et al. [169] reported a mesoporous  $\text{Co}_3\text{O}_4$  nanochains-based  $\text{H}_2\text{S}$  sensor. At first cobalt carbonate hydroxide ( $\text{Co}(\text{CO}_3)_{0.5}(\text{OH})\cdot 11\text{H}_2\text{O}$ ) nanowires were synthesized using a hydrothermal route. Then heat treatment was applied in air at 600 °C for 5 h to form rough-surfaced mesoporous  $\text{Co}_3\text{O}_4$  nanochains as shown by the TEM image in Figure 13D. From the gas responses vs. working temperatures analysis, the optimum working temperature was obtained as 300 °C. At lower operating temperatures than the optimum,  $\text{Co}_3\text{O}_4$  nanochains displayed sluggish chemical activity causing weak responses. Moreover, at higher working temperatures, adsorbed  $\text{H}_2\text{S}$  molecules start escaping from the  $\text{Co}_3\text{O}_4$  nanochain surface because of increased activation. As a result, the sensor response starts decreasing. The fabricated sensor exhibited quick responses and recovery to 1–100 ppm  $\text{H}_2\text{S}$  at 300 °C. At 100 ppm  $\text{H}_2\text{S}$ , response and recovery times were estimated as 46 s and 24 s, respectively, as illustrated in Figure 13E. The nanochain structure provides a high specific surface area, narrow pore size and rich mesopores which make the fabricated sensor more suitable for  $\text{H}_2\text{S}$  sensing than other toxic gases. The comparative responses of  $\text{Co}_3\text{O}_4$  nanochains toward  $\text{H}_2\text{S}$  and other target gases are plotted in Figure 13F indicate strong selectivity for  $\text{H}_2\text{S}$ . Previously, Stanoiu et al. [170] prepared a mesoporous  $\text{SnO}_2\text{-CuWO}_4$ -based cost-effective  $\text{H}_2\text{S}$  sensor having high sensitivity at low working temperature. In addition, a short temperature trigger of 500 °C was applied to enhance the recovery operation of the fabricated sensor.

### 4.3.3. Metal Oxide Microsphere-Based Sensors

Typically, microspheres are small spherical particles having diameters in the micrometer range. Hu et al. [171] reported CuFe<sub>2</sub>O<sub>4</sub> nanoparticles-decorated CuO microspheres-based H<sub>2</sub>S gas sensors. The synthesized CuO/CuFe<sub>2</sub>O<sub>4</sub> heterostructures provided a porous and rough surface due to the arbitrary deposition of nanoparticles as displayed by the FE-SEM image in Figure 14A. When the temperature is low, the response becomes low because of the weak chemical interaction between the gas molecules and adsorbed oxygen species. At higher working temperatures, the mentioned chemical interaction is strong and the responses keep increasing, but gas molecule diffusion becomes slower than the surface interaction causing a decrease of the response again, as illustrated in Figure 14B. The optimal operating temperature was estimated as 240 °C. The dependence of responses of the sensor on H<sub>2</sub>S concentrations is plotted in Figure 14C which exhibits a gradual increasing trend. The response and recovery time of the fabricated CuO/CuFe<sub>2</sub>O<sub>4</sub> sensor were obtained as 31 s and 40 s, respectively, at the optimal operating temperature (240 °C) with good reproducibility and selectivity toward H<sub>2</sub>S gas. In another study, Li et al. [172] prepared SiO<sub>2</sub>@TiO<sub>2</sub> microspheres and then formed Cd<sup>2+</sup>-doped TiO<sub>2</sub> shell-modified ITO electrodes for H<sub>2</sub>S detection. Exploiting the mismatch of energy band levels between TiO<sub>2</sub> shells and induced CdS nanoparticles, this device provided good sensing performances.

### 4.4. MOF-Based H<sub>2</sub>S Sensors

Metal organic frameworks (MOFs) offer highly selective and sensitive detection of H<sub>2</sub>S because of possessing chemical stability, custom tuning of porosity and functionalities, and various pre- or post-synthetic modifications to the structural framework [173]. Guo et al. [174] synthesized a MOF material named as Zr(TBAPy)<sub>5</sub>(TCPP) using a solvothermal method, where Zr is the metal center, and 1,3,6,8-tetra(4-carboxylphenyl) pyrene (TBAPy) and tetrakis(4-carboxyphenyl) porphyrin (TCPP) act as double linkers. The prepared Zr(TBAPy)<sub>5</sub>(TCPP) exhibited well-shaped shuttle structures with a particle size of about 100 nm as seen from the transmission electron microscope (TEM) image (Figure 14D). However, Zr-MOF NU-1000 (synthesized for comparison) exhibited an irregular structure indicating the structural effect of TCPP on the synthesized materials. The FTIR spectrum of Zr(TBAPy)<sub>5</sub>(TCPP) is displayed in Figure 14E. There is a clear shift in the N-H and C=N peak on the addition of S<sup>2-</sup> due to the attachment between S and N in the materials. Fluorescence enhancement of the fabricated Zr(TBAPy)<sub>5</sub>(TCPP) sensor provides a linear trend with the increase of S<sup>2-</sup> concentration as plotted in Figure 14F. The interference effects of other anions such as- SO<sub>4</sub><sup>2-</sup>, CNS<sup>-</sup>, COOH<sup>-</sup>, Br<sup>-</sup>, I<sup>-</sup>, IO<sub>3</sub><sup>-</sup>, F<sup>-</sup>, HSO<sub>3</sub><sup>-</sup>, Cl<sup>-</sup> and NO<sub>3</sub><sup>-</sup> was investigated and the results confirm that Zr(TBAPy)<sub>5</sub>(TCPP) is highly selective for S<sup>2-</sup> sensing. In another study, Dong et al. [175] developed a ZIF-67-derived porous dodecahedra Co<sub>3</sub>O<sub>4</sub> sensor showing enhanced linear trend with H<sub>2</sub>S concentration. The significant improvement in the overall sensing performances is attributed to a high specific surface and the exposed {110} lattice planes of the fabricated structure.

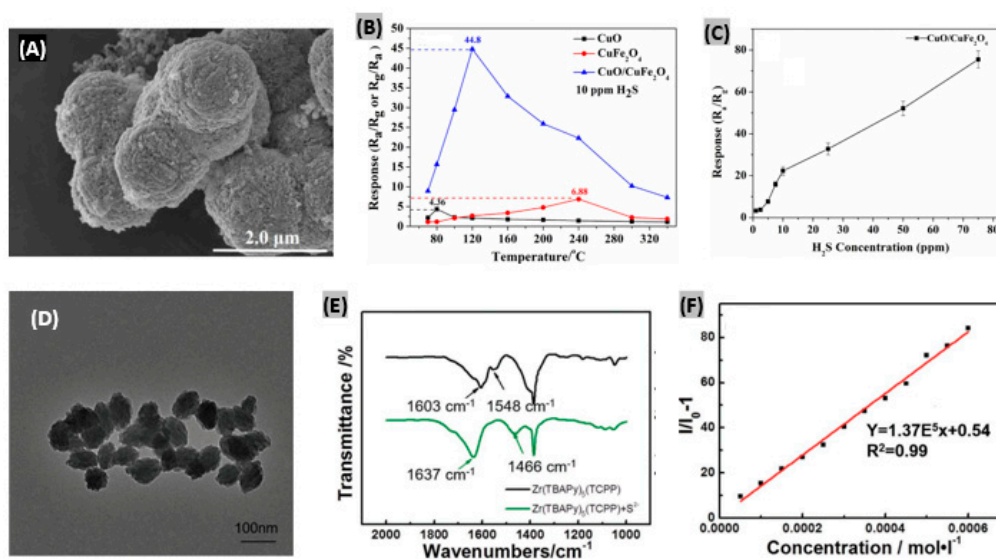


**Figure 14.** (A) FE-SEM image of synthesized CuO/CuFe<sub>2</sub>O<sub>4</sub> heterostructure. (B) Variation of gas sensing responses of CuO microspheres, CuFe<sub>2</sub>O<sub>4</sub> nanoparticles and CuO/CuFe<sub>2</sub>O<sub>4</sub> heterostructure with working temperatures. (C) H<sub>2</sub>S concentrations dependent sensing responses of CuO/CuFe<sub>2</sub>O<sub>4</sub> sensor at 240 °C. Figures adapted with permission from [171], Copyright 2018 Elsevier. (D) TEM image of the synthesized Zr(TBAPy)<sub>5</sub>(TCPP). (E) FTIR spectra of Zr(TBAPy)<sub>5</sub>(TCPP) before and after H<sub>2</sub>S exposure. (F) Fluorescent enhancement response of the fabricated sensor under increasing S<sup>2-</sup> concentration. Figures adapted with permission from [174], Copyright 2018 WILEY-VCH Verlag GmbH & Co. KGaA, Weinheim.

#### 4.5. Organic Materials-Based H<sub>2</sub>S Sensors

In recent years, several attempts have been made for H<sub>2</sub>S sensing using organic semiconducting films and polymers. Different types of interactions like crosslinking, doping, grafting and scissioning between electrons and organic materials take place in subject to energy as well as the dose of incident electron beam [176] which help to attain high selectivity and sensitivity to target gas. Chaudhary et al. reported a polyaniline-silver (PANI-Ag) nanocomposite film-based H<sub>2</sub>S sensor [177]. After protonation of aniline monomers, photopolymerization of aniline on a bi-axially oriented polyethylene terephthalate (BOPET) sheet was performed. The prepared PANI-Ag films were irradiated by a 10 MeV electron beam. As the dose was increased, the nanofiber diameter increased and a 30 kGy dose promoted an interconnected microstructure with larger sized Ag particles. At a very high dose of 100 kGy, Ag clusters submerged inside the polymer matrix with denser structure. The bright spots observed in SEM image as shown in Figure 15A reveal that Ag nanoparticles are incorporated in the PANI matrix. After EB irradiation, Ohmic nature was retained as seen from the linear I-V relationship displayed in Figure 15B. The electrical conductivity kept increasing with the dose to achieve the highest value at 30 kGy and then started going down. The percent sensor responses under different H<sub>2</sub>S concentrations and irradiation doses are plotted in Figure 15C. Since lower irradiation doses cause higher conductivity changes, the corresponding sensing responses become lower upon H<sub>2</sub>S exposure. On the contrary, higher doses cause lower electrical conductivity due to crosslinking-induced structural defects, so, the corresponding sensing responses to H<sub>2</sub>S become larger. Abu-Hani et al. [178] engineered the conductivity of chitosan (CS) film to obtain a highly sensitive and selective sensor toward H<sub>2</sub>S gas. Glycerol ionic liquid (IL) had been incorporated to tune the conductivity of the CS film. It was able to operate at lower temperature and provided rapid response-recovery with low-power consumption. In another study, Cu<sup>2+</sup>-doped SnO<sub>2</sub> nanograin/polypyrrole nanospheres-based H<sub>2</sub>S gas detection was reported [179]. The enhanced sensing performance of the fabricated organic-inorganic nanohybrids is mainly attributed to improved surface potential barrier by surface defects tailoring, and numerous reaction sites to accelerate gas diffusion and adsorption.

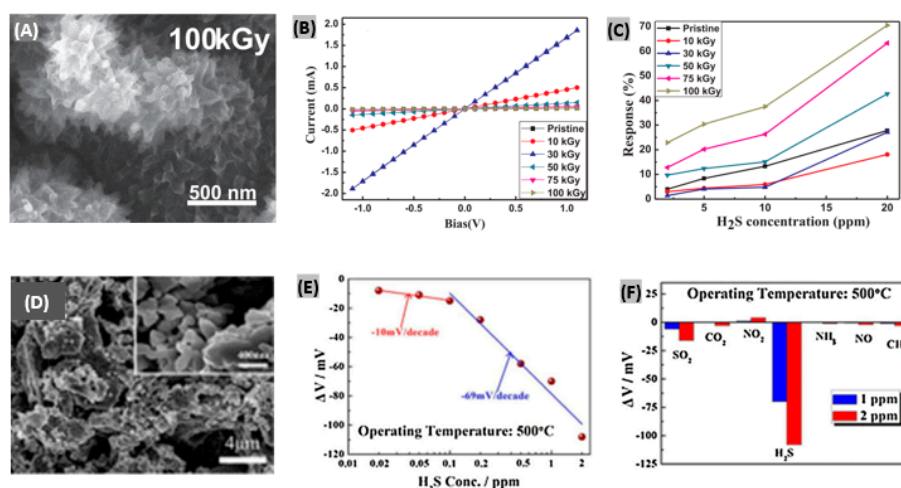


**Figure 15.** (A) FE-SEM image of PANI-Ag film irradiated with EB at 100kGy dose. (B) Current-Voltage relationship of PANI-Ag at pristine and EB irradiated condition. (C) Percent sensor responses under different H<sub>2</sub>S concentrations and irradiation doses. Figures adapted with permission from [177], Copyright 2018 Elsevier. (D) SEM image of LNO-1 sensing electrode (La<sub>2</sub>NiO<sub>4</sub>). (E) Electrode potential difference as a function of the logarithm of H<sub>2</sub>S concentrations (0.02–2 ppm) at 500 °C. (F) Selectivity evaluation of the fabricated sensor at 1 and 2 ppm of every test gas. Figures adapted with permission from [180], Copyright 2017 Elsevier.

#### 4.6. Solid Electrolytes-Based H<sub>2</sub>S Sensors

The mixed potential type sensor requires a solid electrolyte having the ability to transfer oxygen ions between reference electrode and sensing electrode. Hao et al. [180] prepared a mixed-potential H<sub>2</sub>S gas sensor using YSZ as solid electrolyte and La<sub>2</sub>NiO<sub>4</sub> as sensing electrode. The microstructure of the sensing material La<sub>2</sub>NiO<sub>4</sub> was varied with three equivalents of citric acid and total metal irons which were 0.5:1 (LNO-0.5), 1:1 (LNO-1) and 1:2 (LNO-2), respectively. The SEM image of LNO-1 sensing material (La<sub>2</sub>NiO<sub>4</sub> powders) reveals the porous structure and it has the largest pore size among the three samples as displayed in Figure 15D. Also, it was found that LNO-1 possesses the highest BET surface area and pore volume. On increasing the H<sub>2</sub>S exposure concentration, the electrode potential difference exhibited linear changes with the logarithm of H<sub>2</sub>S concentration at 500 °C as plotted in Figure 15E. The sensitivity of the sensor to H<sub>2</sub>S was changed to –10 mV/decade from –69 mV/decade. The recovery time was improved by applying a temperature pulse of 700 °C. For 500 ppb of H<sub>2</sub>S exposure, it decreased from 20 min to 150 s. The fabricated sensor was proved to be highly selective toward H<sub>2</sub>S compared to other target gases as observed from the responses toward 1 and 2 ppm of every test gas (Figure 15F). Moreover, it was found quite stable in long term performance with lower detection limit. In another study, Yang et al. [181] used Nafion as a proton exchange membrane to demonstrate H<sub>2</sub>S sensing with the help of a sensing electrode. The electrode was made of Pt-Rh nanoparticles loaded on carbon fibers. The sensitivity was obtained 0.191 μA/ppm from the linear plot between sensor current changes and corresponding H<sub>2</sub>S concentrations. The fabricated sensor was highly selective toward H<sub>2</sub>S at room temperature with a fast recovery time (16 s) under 50 ppm of gas exposure. Recently, a promising TMD material, WS<sub>2</sub> has been utilized to detect H<sub>2</sub>S with high sensitivity and selectivity [182]. It was observed that oxygen doping in the sulfur sites of the WS<sub>2</sub> lattice promotes enhanced sensing performances towards H<sub>2</sub>S. Earlier, the adsorption properties of WS<sub>2</sub> had been analyzed toward various target gas molecules along with its Fermi level pinning [183]. The sensing performance metrics like sensitivity/response, response and recovery times at certain gas concentration and operating temperatures, and sensitivity per ppm/response time ratio for different H<sub>2</sub>S sensor materials and structures have been summarized in Table 3. It provides a brief comparative performances outline among different H<sub>2</sub>S sensors reported in recent years.

**Table 3.** Gas sensing properties of recently developed H<sub>2</sub>S gas sensors.

Materials	Structure	Operating Temperature (°C)	Concentration (ppm)	Sensitivity/Response	Response Time (s)	Recovery Time (s)	Sensitivity per ppm Response time
In <sub>2</sub> O <sub>3</sub> [184]	Whiskers	RT	10	35	240	7200	0.015
hc-NiO/N-rGO [185]	Composite	92	100	54.06	100	12	0.0054
rGO/hexagonal WO <sub>3</sub> [186]	Nanosheets composite	330	10	45	7	55	0.64
Au/Fe <sub>2</sub> O <sub>3</sub> [187]	Thin films	250	10	6.38	1.65 min	27 min	0.007
α-Fe <sub>2</sub> O <sub>3</sub> [188]	Micro ellipsoids	350	100	11.7	78	15	0.0015
TiO <sub>2</sub> / α-Fe <sub>2</sub> O <sub>3</sub> [189]	Nanorods	300	200	7.4	160	180	2.3 × 10 <sup>-4</sup>
Pd/PdO <sub>x</sub> [190]	Core-shell nanodiscs	200	3	54.9	15	100	1.22
ZnFe <sub>2</sub> O <sub>4</sub> [191]	Nanosheets	85	5	123	39	34	0.63
SnO <sub>2</sub> /ZnO [192]	Net-like hetero nanostructures	100	5	100	513	98	0.04
SnO <sub>2</sub> -CuO [193]	Coral-like nanocomposite	100	100	38	120	long	0.003
CuO-NiO [194]	Core-shell microspheres	260	100	47	18	29	0.026
Cr-doped WO <sub>3</sub> [195]	Microsphere	80	0.1 vol. %	89.3	336	300	2.65
SnO <sub>2</sub> [196]	Multi-tube arrays	RT	5	1.45	14	30	0.02
NiO [197]	Porous nanowall arrays	90	0.001	1.23	49	123	25.1
Cu NPs decorated SWCNTs [198]	Nanotube	RT	5	11%	10	15	0.22
CuO [199]	Porous nanosheets	RT	0.01	1.25	234	76	0.534
PPy-WO <sub>3</sub> [200]	Nanocomposite films	RT	1	81	360	12,600	0.225
SnO <sub>2</sub> -rGO [201]	Nanofibers	200	5	34	120	550	0.06
SnO <sub>2</sub> -rGO [153]	Nanocomposite	125	100	33.02	209	900	0.002
ZnO-C [154]	Composite nanofibers	250	50	102	-	-	-
Pt-gated AlGaIn/GaN [155]	HEMT	250	90	112	219	507	0.006
α-Fe <sub>2</sub> O <sub>3</sub> [164]	Nanosheets	135	5	5.8	10	45	0.116
ZnO/CuO [165]	Nanotube	50	5	25	37	94	0.135
In <sub>2</sub> O <sub>3</sub> [166]	Porous nanoparticles	25	1	26268.5	>200	>200	131.3
Cu <sub>2</sub> O-doped SnO <sub>2</sub> [167]	Nanorod	RT	5	30	21	204	0.29
p-type Co <sub>3</sub> O <sub>4</sub> [169]	Mesoporous nanochains	300	100	4.5	46	24	0.001
SnO <sub>2</sub> -CuWO <sub>4</sub> [170]	Mesoporous layers	100	20	2 × 10 <sup>6</sup> (sensor signal)	2.5 min	7.3 min	-
Chitosan-IL [178]	Film	80	100	200%	>15	-	0.13
Cu <sup>2+</sup> -Doped SnO <sub>2</sub> /Poly pyrrole [179]	Hybrid nanospheres	RT	0.3	9	7	14	4.28

A novel metric, sensitivity per ppm/response time ratio has been calculated for each sensor in order to compare the overall sensing performance on the same reference. The higher value of the calculated ratio indicates the better overall sensor performance. Average ratios have been obtained by taking the recently reported gas sensors into account for the highly focused sensing materials as illustrated in Figure 16. It is found that hybrid materials-based sensors exhibit the highest average ratio for NO<sub>2</sub> gas sensing, whereas GaN and Metal-oxide based sensors possess the highest ratio for SO<sub>2</sub> and H<sub>2</sub>S gas sensing respectively.

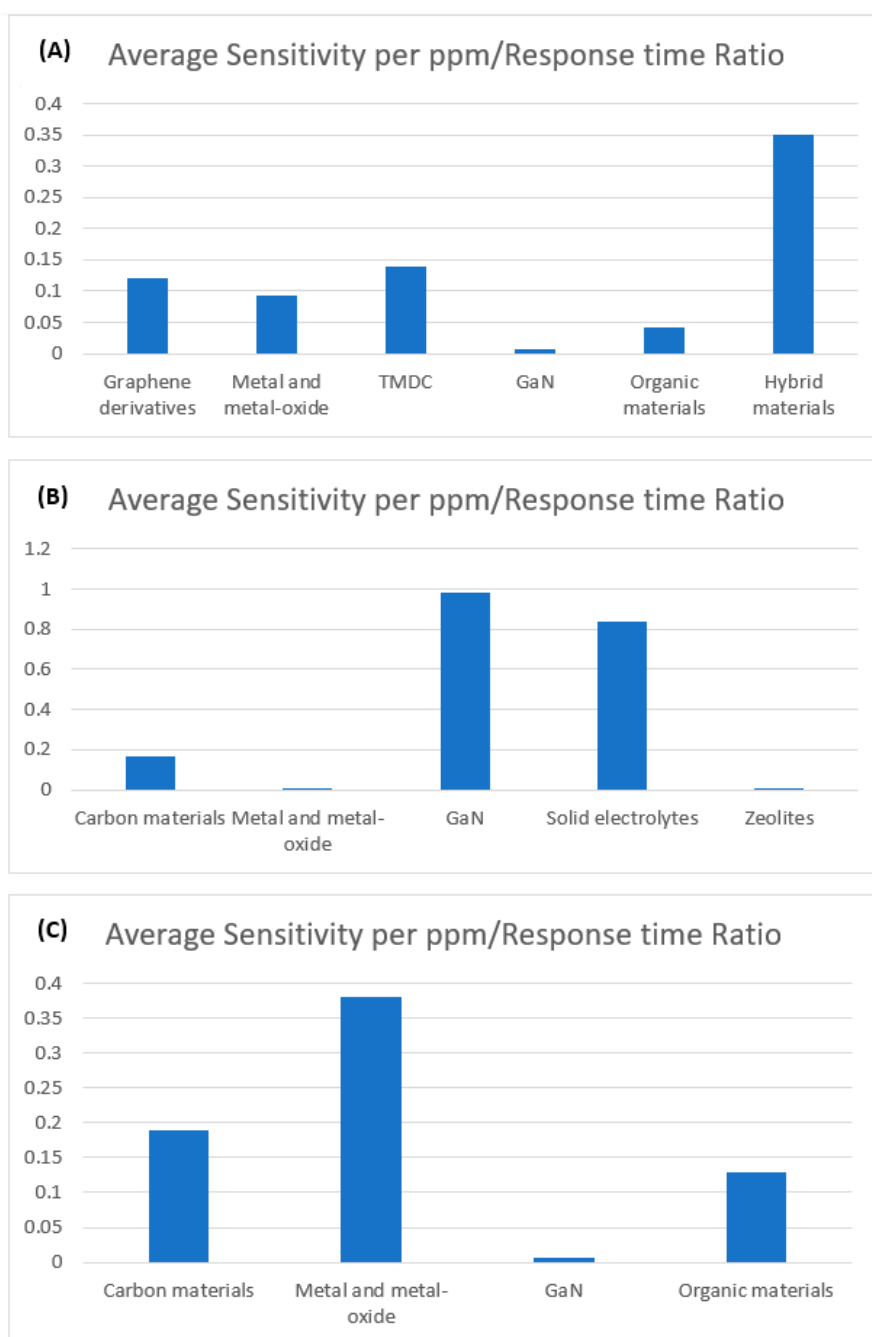


**Figure 16.** Average sensitivity per ppm/response time ratio comparison among various sensing materials reported in recent years for (A) NO<sub>2</sub> (B) SO<sub>2</sub> and (C) H<sub>2</sub>S gas sensors.

## 5. Recent Density-Functional Theory (DFT) Study of Gas Molecule-Sensor Interaction

Numerous efforts have been made to investigate the adsorption properties of various sensing materials toward different toxic gases including NO<sub>2</sub>, SO<sub>2</sub> and H<sub>2</sub>S by first-principle method calculations using density functional theory (DFT) in recent years as shown in Table 4.

For instance, Chen et al. [202] reported that NO<sub>2</sub> and SO<sub>2</sub> adsorptions show chemisorption character on boron-doped arsenene whereas physisorption character on pristine and nitrogen-doped arsenene. Mao et al. [203] explored the effect of Ge/Se vacancy, anti-site defect, and P atom substituted defect on GeSe monolayer toward toxic gas adsorption. It was found that, the point defect engineering alters electronic structure and work function of GeSe monolayer and thus influence on the adsorption properties of target gas molecules. Besides, adsorption properties such as- adsorption energy, shortest adsorption distance, charge transfer estimation, stability etc. toward NO<sub>2</sub>, SO<sub>2</sub> and H<sub>2</sub>S have been studied based on various sensing materials like borophene [204], monolayer C<sub>3</sub>N [205], blue phosphorene [206], organolithium (C<sub>2</sub>H<sub>4</sub>Li) complex [207], Ni-MoS<sub>2</sub> monolayer [208], germanene nanosheet (Ge-NS) [209], Fe-atom-functionalized CNTs [210], 2D tetragonal GaN [211], graphitic GaN sheet [212], etc.

**Table 4.** The adsorption energy (eV), Shortest adsorption distance (Å) and charge transfer (e) between NO<sub>2</sub>, SO<sub>2</sub>, H<sub>2</sub>S and various sensing materials at the most stable adsorption configuration based on DFT.

Materials	Target Gas	Adsorption Energy (eV)	Shortest Adsorption Distance (Å)	Charge Transfer (e)
Pristine Arsenene [202]	NO <sub>2</sub>	−0.4378	2.955	−0.187
B-doped Arsenene [202]	NO <sub>2</sub>	−1.913	1.562	−0.273
N-doped Arsenene [202]	NO <sub>2</sub>	−0.4502	2.506	−0.163
Pristine Arsenene [202]	SO <sub>2</sub>	−0.3413	2.957	−0.192
B-doped Arsenene [202]	SO <sub>2</sub>	−1.0733	1.961	−0.141
N-doped Arsenene [202]	SO <sub>2</sub>	−0.8597	2.278	−0.251
GeSe monolayer (Ge <sub>Top</sub> ) [203]	SO <sub>2</sub>	−0.58	2.86	−0.2788
GeSe monolayer (Ge <sub>Top</sub> ) [203]	NO <sub>2</sub>	−2.24	2.29	−0.464
GeSe monolayer (Se <sub>Top</sub> ) [203]	SO <sub>2</sub>	−0.52	2.84	−0.2321
GeSe monolayer (Se <sub>Top</sub> ) [203]	NO <sub>2</sub>	−1.97	3.09	−0.2505
Borophene (buckled) [204]	NO <sub>2</sub>	1.75	1.56	0.76
Borophene (line-defective) [204]	NO <sub>2</sub>	1.80	1.57	0.89
Monolayer C <sub>3</sub> N [205]	NO <sub>2</sub>	−0.79	2.89	−0.388
Monolayer C <sub>3</sub> N [205]	H <sub>2</sub> S	−0.23	3.39	−0.004
Monolayer C <sub>3</sub> N [205]	SO <sub>2</sub>	−0.62	2.84	−0.247
Blue Phosphorene [206]	H <sub>2</sub> S	−0.242	3.2	0.037
Blue Phosphorene [206]	SO <sub>2</sub>	−0.247	3.0	−0.138
C <sub>2</sub> H <sub>4</sub> Li [207]	NO <sub>2</sub>	4.07	1.90	−0.77
C <sub>2</sub> H <sub>4</sub> Li [207]	SO <sub>2</sub>	3.09	1.90	−0.38
Ni-MoS <sub>2</sub> monolayer [208]	H <sub>2</sub> S	−1.319	2.205	0.254
Ni-MoS <sub>2</sub> monolayer [208]	SO <sub>2</sub>	−1.382	2.059	−0.016
2D Tetragonal GaN [211]	NO <sub>2</sub>	−0.673	2.066	−0.108
Graphitic GaN sheet [212]	NO <sub>2</sub>	−0.493	2.44	−0.081
Graphitic GaN sheet [212]	SO <sub>2</sub>	−1.06	1.79	−0.209
Graphitic GaN sheet [212]	H <sub>2</sub> S	−0.446	2.89	0.139

## 6. Calibration of Toxic Gas Sensors

In order to check sensor precision, toxic gas sensors must be calibrated at regular intervals. The sensor producers typically suggest a time interval between calibrations. Single toxic gas detectors are normally calibrated with a defined toxic gas depending on the gas type whereas multi-gas detectors are calibrated with their own specific calibration gas mixtures. There are mainly two steps in the gas sensor calibration. Firstly, a reference zero reading must be established using pure nitrogen or pure synthetic air. Secondly, the sensor operating range must be calibrated using a standard gas mixture. The ideal practice is to apply a mixture of the target gas balanced in the natural air as the calibration

gas. Premixed calibration gas, permeation devices, cross calibration, gas mixing, Gaussian processes are some of the practical methods of calibrating the gas sensors [213–215].

## 7. Toxic Gas Sensors in Internet of Things (IoT) Applications

The Internet of Things is a network of physical objects that utilizes sensors and application programming interfaces (APIs) to collect and exchange data over the internet. IoT network requires ultra-low power, low cost, long lifetime, integrable into electronic circuits, and mini-sized gas sensors for remote air quality monitoring and enhanced automated system [216]. Electrochemical gas sensors can provide these characteristics required by IoT platforms, thus become suitable candidate for the IoT applications such as creating smart environment, smart home, smart parking system and so on [217,218]. Toxic gas sensors were incorporated into a multi-purpose field surveillance robot which uses multiple IoT cloud servers [219]. High performance gas sensors are utilized in IoT-based vehicle emission monitoring systems [220]. Besides, wireless sensor networks have been employed for toxic gas boundary area detection in large-scale petrochemical plants [221]. However, the gas sensing performances are strongly affected by miniaturization of sensor in terms of length and width between the electrodes, number of electrodes, sensing area etc. [222]. Extensive studies on sensing properties of miniaturized gas sensors can further facilitate the implementation of toxic gas sensors in IoT platforms.

## 8. Future Perspectives and Conclusions

Toxic gas sensors play an important role in many aspects of technology, industry, or daily life. In recent years, researchers have exploited the fundamental properties of various gas sensing materials to achieve high performance toxic gas sensors. Particularly, excellent improvements have been attained in terms of sensitivity, selectivity, limit of detection, miniaturization and portability for NO<sub>2</sub>, SO<sub>2</sub> and H<sub>2</sub>S gas sensors using novel combination of nanomaterials exhibiting various morphologies. However, the toxic gas sensors reported so far have limitations in some of the important performance metrics, such as- response and recovery times, stability, operating temperature, reproducibility, fabrication cost, reliability etc. These limitations can be overcome by further exploiting the hybrid and heterostructure, exploring more in surface functionalization, and adopting novel, efficient and cost-effective fabrication technique. This work reviews and categorizes the recent progress in electrochemical detection of NO<sub>2</sub>, SO<sub>2</sub> and H<sub>2</sub>S gases based on various highly explored sensing materials over the past few decades. Moreover, the sensing performance parameters like sensitivity/ response, response and recovery times at certain gas exposure concentration and operating temperature for various sensor materials and structures have been tabulated which provide a brief comparative performances outline to the reader. This study will give an overview on the research trend of the above-mentioned toxic gas sensors to the current and future researchers.

**Acknowledgments:** The authors M.A.H.K. and M.V.R. would like to acknowledge the support of NSF grant: 204541. Q.L. would like to acknowledge the support of a Virginia Microelectronics Consortium research grant.

**Conflicts of Interest:** The authors declare no conflict of interest. The funders had no role in the design of the study; in the collection, analyses, or interpretation of data; in the writing of the manuscript, or in the decision to publish the results.

## References

1. Anenberg, S.C.; Miller, J.; Minjares, R.; Du, L.; Henze, D.K.; Lacey, F.; Malley, C.S.; Emberson, L.; Franco, V.; Klimont, Z.; et al. Impacts and mitigation of excess diesel-related NO<sub>x</sub> emissions in 11 major vehicle markets. *Nature* **2017**, *545*, 467–471. [[CrossRef](#)] [[PubMed](#)]
2. Boleij, J.S.M.; Ruigewaard, P.; Hoek, F.; Thairu, H.; Wafula, E.; Onyango, F.; de Koning, H. Domestic air pollution from biomass burning in Kenya. *Atmos. Environ.* **1989**, *23*, 1677–1681. [[CrossRef](#)]
3. Robinson, E.; Robbins, R.C. Gaseous Nitrogen Compound Pollutants from Urban and Natural Sources. *J. Air Pollut. Control Assoc.* **1970**, *20*, 303–306. [[CrossRef](#)]

4. Bauer, M.A.; Utell, M.J.; Morrow, P.E.; Speers, D.M.; Gibb, F.R. Inhalation of 0.30 ppm nitrogen dioxide potentiates exercise-induced bronchospasm in asthmatics. *Am. Rev. Respir. Dis.* **1986**, *134*, 1203–1208. [[PubMed](#)]
5. Ehrlich, R. Effect of nitrogen dioxide on resistance to respiratory infection. *Bacteriol. Rev.* **1966**, *30*, 604–614. [[PubMed](#)]
6. Genc, S.; Zadeoglulari, Z.; Fuss, S.H.; Genc, K. The adverse effects of air pollution on the nervous system. *J. Toxicol.* **2012**, *2012*. [[CrossRef](#)]
7. Lee, S.W.; Lee, W.; Hong, Y.; Lee, G.; Yoon, D.S. Recent advances in carbon material-based NO<sub>2</sub> gas sensors. *Sens. Actuators B Chem.* **2018**, *255*, 1788–1804. [[CrossRef](#)]
8. Guo, Y.Y.; Li, Y.R.; Zhu, T.Y.; Ye, M. Investigation of SO<sub>2</sub> and NO adsorption species on activated carbon and the mechanism of NO promotion effect on SO<sub>2</sub>. *Fuel* **2015**, *143*, 536–542. [[CrossRef](#)]
9. Chatterjee, C.; Sen, A. Sensitive colorimetric sensors for visual detection of carbon dioxide and sulfur dioxide. *J. Mater. Chem. A* **2015**, *3*, 5642–5647. [[CrossRef](#)]
10. Khan, R.R.; Siddiqui, M.J.A. Review on effects of Particulates; Sulfur Dioxide and Nitrogen Dioxide on Human Health. *Int. Res. J. Environment Sci.* **2014**, *3*, 70–73.
11. Nisar, J.; Topalian, Z.; Sarkar, A.D.; Osterlund, L.; Ahuja, R. TiO<sub>2</sub>-based gas sensor: A possible application to SO<sub>2</sub>. *ACS Appl. Mater. Interfaces* **2013**, *5*, 8516–8522. [[CrossRef](#)]
12. Zeng, Y.; Zhang, K.; Wang, X.; Sui, Y.; Zou, B.; Zheng, W.; Zou, G. Rapid and selective H<sub>2</sub>S detection of hierarchical ZnSnO<sub>3</sub> nanocages. *Sens. Actuators B Chem.* **2011**, *159*, 245–250. [[CrossRef](#)]
13. Bari, H.R.; Patil, P.P.; Patil, S.B.; Bari, A.R. Detection of H<sub>2</sub>S gas at lower operating temperature using sprayed nanostructured In<sub>2</sub>O<sub>3</sub> thin films. *Bull. Mater. Sci.* **2013**, *36*, 967–972. [[CrossRef](#)]
14. Chou, C. *Hydrogen Sulfide: Human Health Aspects: Concise International Chemical Assessment Document 53*; World Health Organization: Geneva, Switzerland, 2003.
15. Wiheeb, A.D.; Shamsudin, I.K.; Ahmad, M.A.; Murat, M.N.; Kim, J.; Othman, M.R. Present Technologies for Hydrogen Sulfide Removal from Gaseous Mixtures. *Rev. Chem. Eng.* **2013**, *29*, 449–470. [[CrossRef](#)]
16. Levitsky, I.A. Porous Silicon Structures as Optical Gas Sensors. *Sensors* **2015**, *15*, 19968–19991. [[CrossRef](#)] [[PubMed](#)]
17. Hök, B.; Blücker, A.; Löfving, J. Acoustic gas sensor with ppm resolution. *Sens. Rev.* **2000**, *20*, 139–142. [[CrossRef](#)]
18. Li, M.; Myers, E.B.; Tang, H.X.; Aldridge, S.J.; McCaig, H.C.; Whiting, J.J.; Simonson, R.J.; Lewis, N.S.; Roukes, M.L. Nanoelectromechanical Resonator Arrays for Ultrafast, Gas-Phase Chromatographic Chemical Analysis. *Nano Lett.* **2010**, *10*, 3899–3903. [[CrossRef](#)]
19. Yunusa, Z.; Hamidon, M.N.; Kaiser, A.; Awang, Z. Gas Sensors: A Review. *Sens. Transducers* **2014**, *168*, 61–75.
20. Schedin, F.; Geim, A.K.; Morozov, S.V.; Hill, E.W.; Blake, P.; Katsnelson, M.I.; Novoselov, K.S. Detection of individual gas molecules adsorbed on graphene. *Nat. Mater.* **2007**, *6*, 652–655. [[CrossRef](#)]
21. Ko, G.; Kim, H.Y.; Ahn, J.; Park, Y.M.; Lee, K.Y.; Kim, J. Graphene-based nitrogen dioxide gas sensors. *Curr. Appl. Phys.* **2010**, *10*, 1002–1004. [[CrossRef](#)]
22. Iqbal, N.; Afzal, A.; Cioffi, N.; Sabbatini, L.; Torsi, L. NO<sub>x</sub> sensing one- and two-dimensional carbon nanostructures and nanohybrids: Progress and perspectives. *Sens. Actuators B Chem.* **2013**, *181*, 9–21. [[CrossRef](#)]
23. Yuan, W.; Shi, G. Graphene-based gas sensors. *J. Mater. Chem. A* **2013**, *1*, 10078–10091. [[CrossRef](#)]
24. Ren, Y.; Zhu, C.; Cai, W.; Li, H.; Ji, H.; Kholmanov, I.; Wu, Y.; Piner, R.D. Ruoff RS Detection of sulfur dioxide gas with graphene field effect transistor. *Appl. Phys. Lett.* **2012**, *100*, 163114. [[CrossRef](#)]
25. Rana, M.M.; Ibrahim, D.S.; Asyraf, M.R.M.; Jarin, S.; Tomal, A. A review on recent advances of CNTs as gas sensors. *Sens. Rev.* **2017**, *37*, 127–136. [[CrossRef](#)]
26. Kumar, D.; Chaturvedi, P.; Saho, P.; Jha, P.; Chouksey, A.; Lal, M.; Rawat, J.S.B.S.; Tandon, R.P.; Chaudhury, P.K. Effect of single wall carbon nanotube networks on gas sensor response and detection limit. *Sens. Actuators B Chem.* **2017**, *240*, 1134–1140. [[CrossRef](#)]
27. Kang, I.-S.; So, H.-M.; Bang, G.-S.; Kwak, J.-H.; Lee, J.-O.; Won Ahn, C. Recovery improvement of graphene-based gas sensors functionalized with nanoscale heterojunctions. *Appl. Phys. Lett.* **2012**, *101*, 123504. [[CrossRef](#)]
28. Chen, G.; Paronyan, T.M.; Pigos, E.M.; Harutyunyan, A.R. Enhanced gas sensing in pristine carbon nanotubes under continuous ultraviolet light illumination. *Sci. Rep.* **2012**, *2*, 343. [[CrossRef](#)]

29. Ye, H.; Nallon, E.C.; Schnee, V.P.; Shi, C.; Jiang, K.; Xu, J.; Feng, S.; Wang, H.; Li, Q. Enhance the Discrimination Precision of Graphene Gas Sensors with a Hidden Markov Model. *Anal. Chem.* **2018**, *90*, 13790–13795. [[CrossRef](#)]
30. Pearce, R.; Iakimov, T.; Andersson, M.; Hultman, L.; Spetz, A.L.; Yakimova, R. Epitaxially grown graphene based gas sensors for ultra-sensitive NO<sub>2</sub> detection. *Sens. Actuators B Chem.* **2011**, *155*, 451–455. [[CrossRef](#)]
31. Nallon, E.C.; Schnee, V.P.; Bright, C.; Polcha, M.P.; Li, Q. Chemical Discrimination with an Unmodified Graphene Chemical Sensor. *ACS Sens.* **2016**, *1*, 26–31. [[CrossRef](#)]
32. Esmaeilzadeh, J.; Marzbanrad, E.; Zamani, C.; Raissi, B. Fabrication of undoped-TiO<sub>2</sub> nanostructure-based NO<sub>2</sub> high temperature gas sensor using low frequency AC electrophoretic deposition method. *Sens. Actuators B Chem.* **2012**, *161*, 401–405. [[CrossRef](#)]
33. Shubhda, S.; Kiran, J.; Singh, V.N.; Sukhvir, S.; Vijayan, N.; Nita, D.; Gupta, G.; Senguttuvan, T.D. Faster response of NO<sub>2</sub> sensing in graphene–WO<sub>3</sub> nanocomposites. *Nanotechnology* **2012**, *23*, 205501.
34. Wang, Y.; Jiang, X.; Xia, Y. Precursor Route to Polycrystalline SnO<sub>2</sub> Nanowires That Can Be Used for Gas Sensing under Ambient Conditions. *J. Am. Chem. Soc.* **2003**, *125*, 16176–16177. [[CrossRef](#)] [[PubMed](#)]
35. Xue, X.; Xing, L.; Chen, Y.; Shi, S.; Wang, Y.; Wang, T. Synthesis and H<sub>2</sub>S Sensing Properties of CuO-SnO<sub>2</sub> Core/Shell PN-Junction Nanorods. *J. Phys. Chem. C* **2008**, *112*, 12157–12160. [[CrossRef](#)]
36. Domènech-Gil, G.; Barth, S.; Samà, J.; Pellegrino, P.; Gràcia, I.; Cané, C.; Romano-Rodríguez, A. Gas sensors based on individual indium oxide nanowire. *Sens. Actuators B Chem.* **2017**, *238*, 447–454. [[CrossRef](#)]
37. Young-Jin, C.; In-Sung, H.; Jae-Gwan, P.; Jin, C.K.; Jae-Hwan, P.; Jong-Heun, L. Novel fabrication of an SnO<sub>2</sub> nanowire gas sensor with high sensitivity. *Nanotechnology* **2008**, *19*, 095508.
38. Shi, C.; Ye, H.; Wang, H.; Ioannou, D.E.; Li, Q. Precise gas discrimination with cross-reactive graphene and metal oxide sensor arrays. *Appl. Phys. Lett.* **2018**, *113*, 222102. [[CrossRef](#)]
39. Lee, K.; Gatensby, R.; McEvoy, N.; Hallam, T.; Duesberg, G.S. High-Performance Sensors Based on Molybdenum Disulfide Thin Films. *Adv. Mater.* **2013**, *25*, 6699–6702. [[CrossRef](#)]
40. Shokri, A.; Salami, N. Gas sensor based on MoS<sub>2</sub> monolayer. *Sens. Actuators B Chem.* **2016**, *236*, 378–385. [[CrossRef](#)]
41. Liu, B.; Chen, L.; Liu, G.; Abbas, A.N.; Fathi, M.; Zhou, C. High Performance Chemical Sensing Using Schottky-Contacted Chemical Vapor Deposition Grown Monolayer MoS<sub>2</sub> Transistors. *ACS Nano* **2014**, *8*, 5304–5314. [[CrossRef](#)]
42. Schalwig, J.; Muller, G.; Eickhoff, M.; Ambacher, O.; Stutzmann, M. Gas sensitive GaN/AlGaIn-heterostructures. *Sens. Actuators B Chem.* **2002**, *87*, 425–430. [[CrossRef](#)]
43. Makoto, M.; Shu, F.; Takashi, E. Demonstration of NO<sub>x</sub> gas sensing for Pd/ZnO/GaN heterojunction diodes. *J. Vac. Sci. Technol.* **2015**, *33*, 013001.
44. Song, J.; Lu, W.; Flynn, J.; Brandes, G. Pt-AlGaIn/GaN Schottky diodes operated at 800 °C for hydrogen sensing. *Appl. Phys. Lett.* **2005**, *87*, 133501. [[CrossRef](#)]
45. Tilak, V.; Matocha, K.; Sandvik, P. Pt/GaN Schottky diodes for harsh environment NO sensing applications. *Phys. Status Solidi* **2005**, *7*, 2555–2558. [[CrossRef](#)]
46. Das, A.; Dost, R.; Richardson, T.; Grell, M.; Morrison, J.J.; Turner, M.L. A nitrogen dioxide sensor based on an organic transistor constructed from amorphous semiconducting polymers. *Adv. Mater.* **2007**, *19*, 4018–4023. [[CrossRef](#)]
47. Agbor, N.E.; Petty, M.C.; Monkman, A.P. Polyaniline thin films for gas sensing. *Sens. Actuators B Chem.* **1995**, *28*, 173–179. [[CrossRef](#)]
48. Yuan, W.; Huang, L.; Zhou, Q.; Shi, G. Ultrasensitive and selective nitrogen dioxide sensor based on self-Assembled Graphene/Polymer composite nanofibers. *ACS Appl. Mater. Interfaces* **2014**, *6*, 17003–17008. [[CrossRef](#)]
49. Mekki, A.; Joshi, N.; Singh, A.; Salmi, Z.; Jha PDecorse, P.; Lau-Truong, S.; Mahmoud, R.; Chehimi, M.M.; Aswal, D.K.; Gupta, S.K. H<sub>2</sub>S sensing using in situ photopolymerized polyaniline-silver nanocomposite films on flexible substrates. *Org. Electron.* **2014**, *15*, 71–81. [[CrossRef](#)]
50. Hyodo, T.; Sasahara, K.; Shimizu, Y.; Egashira, M. Preparation of microporous SnO<sub>2</sub> films using PMMA microspheres and their sensing properties to NO<sub>x</sub> and H<sub>2</sub>. *Sens. Actuators B Chem.* **2005**, *106*, 580–590.
51. Liang, X.; Zhong, T.; Quan, B.; Wang, B.; Guan, H. Solid-state potentiometric SO<sub>2</sub> sensor combining NASICON with V<sub>2</sub>O<sub>5</sub>-doped TiO<sub>2</sub> electrode. *Sens. Actuators B Chem.* **2008**, *134*, 25–30. [[CrossRef](#)]

52. Giang, H.T.; Duy, H.T.; Ngan, P.Q.; Thai, G.H.; Thu, D.T.A.; Thu, D.T.; Toan, N.N. High sensitivity and selectivity of mixed potential sensor based on Pt/YSZ/SmFeO<sub>3</sub> to NO<sub>2</sub> gas. *Sens. Actuators B Chem.* **2013**, *183*, 550–555. [[CrossRef](#)]
53. Guan, Y.; Yin, C.; Cheng, X.; Liang, X.; Diao, Q.; Zhang, H.; Lu, G. Sub-ppm H<sub>2</sub>S sensor based on YSZ and hollow balls NiMn<sub>2</sub>O<sub>4</sub> sensing electrode. *Sens. Actuators B Chem.* **2014**, *193*, 501–508. [[CrossRef](#)]
54. Min, B.; Choi, S. SO<sub>2</sub>-sensing characteristics of NASICON sensors with Na<sub>2</sub>SO<sub>4</sub>–BaSO<sub>4</sub> auxiliary electrolytes. *Sens. Actuators B Chem.* **2003**, *93*, 209–213. [[CrossRef](#)]
55. Marcu, I.C.; Sandulescu, I. Study of sulfur dioxide adsorption on Y zeolite. *J. Serb. Chem. Soc.* **2004**, *69*, 563–569. [[CrossRef](#)]
56. Xu, X.; Wang, J.; Long, Y. Zeolite-based materials for gas sensors. *Sensors* **2006**, *6*, 1751–1764. [[CrossRef](#)]
57. Mohan, K.J.; Jagadeesan, K.; Yadav, A. A novel approach for zeolite-based materials for gas sensors. *IOSR J. Environ. Sci. Toxicol. Food Technol.* **2013**, *6*, 1–5. [[CrossRef](#)]
58. Dragan, G. The simultaneous adsorption of sulphur dioxide and carbon dioxide by Y zeolites. *Rev. Chim.* **2010**, *61*, 1071–1075.
59. Ma, J.M.; Mei, L.; Chen, Y.J.; Li, Q.H.; Wang, T.H.; Xu, Z.; Duan, X.C.; Zheng, W.J. Ammonium acetate-based ionothermal synthesis and ultrasensitive sensors for low-ppm-level H<sub>2</sub>S gas. *Nanoscale* **2013**, *5*, 895–898. [[CrossRef](#)]
60. Swain, S.K.; Barik, S.; Das, R. Nanomaterials as Sensor for Hazardous Gas Detection. In *Handbook of Ecomaterials*; Martínez, L., Kharissova, O., Kharisov, B., Eds.; Springer: Cham, Switzerland, 2018.
61. Hoffmann, M.W.G.; Casals, O.; Gad, A.E.; Mayrhofer, L.; Caccamo, C.F.L.; Hernández-Ramírez, F.; Lilienkamp, G.; Daum, W.; Moseler, M.; Shen, H.; et al. Novel Approaches towards Highly Selective Self-Powered Gas Sensors. *Procedia Eng.* **2015**, *120*, 623–627. [[CrossRef](#)]
62. Lahade, S.V.; Pardhi, P.D. Gas Sensing Technologies: Review, Scope and Challenges. *Int. J. Recent Trends Eng. Res.* **2018**, *4*, 108–115.
63. Sharma, S.; Madou, M. Review: A new approach to gas sensing with nanotechnology. *Phil. Trans. R. Soc. A* **2012**, *370*, 2448–2473. [[CrossRef](#)] [[PubMed](#)]
64. Yuan, W.J.; Liu, A.R.; Huang, L.; Li, C.; Shi, G.Q. High Performance NO<sub>2</sub> Sensors Based on Chemically Modified Graphene. *Adv. Mater.* **2013**, *25*, 766–771. [[CrossRef](#)] [[PubMed](#)]
65. Duy, L.T.; Kim, D.-J.; Trung, T.Q.; Dang, V.Q.; Kim, B.-Y.; Moon, H.K.; Lee, N.-E. High Performance Three-Dimensional Chemical Sensor Platform Using Reduced Graphene Oxide Formed on High Aspect-Ratio Micro-Pillars. *Adv. Funct. Mater.* **2015**, *25*, 883–890. [[CrossRef](#)]
66. Melios, C.; Panchal, V.; Edmonds, K.; Lartsev, A.; Yakimova, R.; Kazakova, O. Detection of ultra-low concentration NO<sub>2</sub> in complex environment using epitaxial graphene sensors. *ACS Sens.* **2018**, *3*, 1666–1674. [[CrossRef](#)] [[PubMed](#)]
67. Wang, Z.; Zhang, T.; Zhao, C.; Han, T.; Fei, T.; Liu, S.; Lu, G. Anchoring ultrafine Pd nanoparticles and SnO<sub>2</sub> nanoparticles on reduced graphene oxide for high-performance room temperature NO<sub>2</sub> sensing. *J. Colloid Interface Sci.* **2018**, *514*, 599–608. [[CrossRef](#)] [[PubMed](#)]
68. Opalka, S.M.; Løvvik, O.M.; Emerson, S.C.; She, Y.; Vanderspurt, T.H. Electronic origins for sulfur interactions with palladium alloys for hydrogen-selective membranes. *J. Membr. Sci.* **2011**, *375*, 96–103. [[CrossRef](#)]
69. Wang, Z.; Zhang, T.; Han, T.; Fei, T.; Liu, S.; Lu, G. Oxygen vacancy engineering for enhanced sensing performances: A case of SnO<sub>2</sub> nanoparticles-reduced graphene oxide hybrids for ultrasensitive ppb-level room-temperature NO<sub>2</sub> sensing. *Sens. Actuators B Chem.* **2018**, *266*, 812–822. [[CrossRef](#)]
70. Akbari, E.; Buntat, Z.; Iqbal, S.M.Z.; Azman, Z.; Sahari, N.; Nawawi, Z.; Jambak, M.I.; Sidik, M.A.B. NO<sub>2</sub> Gas Sensing Properties of Carbon Films Fabricated by Arc Discharge Methane Decomposition Technique. *TELKOMNIKA* **2018**, *16*, 69–76. [[CrossRef](#)]
71. Zhang, H.; Li, Q.; Huang, J.; Du, Y.; Ruan, S.C. Reduced Graphene Oxide/Au Nanocomposite for NO<sub>2</sub> Sensing at Low Operating Temperature. *Sensors* **2016**, *16*, 1152. [[CrossRef](#)] [[PubMed](#)]
72. Manzeli, S.; Ovchinnikov, D.; Pasquier, D.; Yazyev, O.V.; Kis, A. 2D transition metal dichalcogenides. *Nat. Rev. Mater.* **2017**, *2*, 17033. [[CrossRef](#)]
73. Perkins, F.K.; Friedman, A.L.; Cobas, E.; Campbell, P.M.; Jernigan, G.G.; Jonker, B.T. Chemical Vapor Sensing with Monolayer MoS<sub>2</sub>. *Nano Lett.* **2013**, *13*, 668–673. [[CrossRef](#)] [[PubMed](#)]
74. Yang, S.; Jiang, C.; Wei, S.H. Gas sensing in 2D materials. *Appl. Phys. Rev.* **2017**, *4*, 021304. [[CrossRef](#)]

75. Cho, B.; Hahm, M.G.; Choi, M.; Yoon, J.; Kim, A.R.; Lee, Y.-J.; Park, S.-G.; Kwon, J.-D.; Kim, C.S.; Song, M.; et al. Charge transfer-based Gas Sensing Using Atomic-layer MoS<sub>2</sub>. *Sci. Rep.* **2015**, *5*, 8052. [[CrossRef](#)] [[PubMed](#)]
76. Agrawal, A.V.; Kumar, R.; Venkatesan, S.; Zakhidov, A.; Yang, G.; Bao, J.; Kumar, M.; Kumar, M. Photoactivated Mixed In-Plane and Edge-Enriched p-Type MoS<sub>2</sub> Flake-Based NO<sub>2</sub> Sensor Working at Room Temperature. *ACS Sens.* **2018**, *3*, 998–1004. [[CrossRef](#)] [[PubMed](#)]
77. Kumar, R.; Goel, N.; Kumar, M. High performance NO<sub>2</sub> sensor using MoS<sub>2</sub> nanowires network. *Appl. Phys. Lett.* **2018**, *112*, 053502. [[CrossRef](#)]
78. Choi, S.Y.; Kim, Y.; Chung, H.-S.; Kim, A.R.; Kwon, J.-D.; Park, J.; Kim, Y.L.; Kwon, S.; Hahm, M.G.; Cho, B. Effect of Nb Doping on Chemical Sensing Performance of Two-Dimensional Layered MoSe<sub>2</sub>. *ACS Appl. Mater. Interfaces* **2017**, *9*, 3817–3823. [[CrossRef](#)] [[PubMed](#)]
79. Ko, K.Y.; Song, J.-G.; Kim, Y.; Choi, T.; Shin, S.; Lee, C.W.; Lee, K.; Koo, J.; Lee, H.; Kim, J.; et al. Improvement of Gas-Sensing Performance of Large-Area Tungsten Disulfide Nanosheets by Surface Functionalization. *ACS Nano* **2016**, *10*, 9287–9296. [[CrossRef](#)]
80. Gönüllü, Y.; Rodríguez, G.C.M.; Saruhan, B.; Ürgen, M. Improvement of gas sensing performance of TiO<sub>2</sub> towards NO<sub>2</sub> by nano-tubular structuring. *Sens. Actuators B Chem.* **2012**, *169*, 151–160. [[CrossRef](#)]
81. Vyas, R.; Sharma, S.; Gupta, P.; Vijay, Y.K.; Prasad, A.K.; Tyagi, A.K.; Sachdev, K.; Sharma, S.K. Enhanced NO<sub>2</sub> sensing using ZnO–TiO<sub>2</sub> nanocomposite thin films. *J. Alloy. Compd.* **2013**, *554*, 59–63. [[CrossRef](#)]
82. Zhang, J.; Zeng, D.; Zhu, Q.; Wu, J.; Huang, Q.; Xie, C. Effect of Nickel Vacancies on the Room-Temperature NO<sub>2</sub> Sensing Properties of Mesoporous NiO Nanosheets. *J. Phys. Chem. C* **2016**, *120*, 3936–3945. [[CrossRef](#)]
83. Postica, V.; Gröttrup, J.; Adelung, R.; Lupan, O.; Mishra, A.K.; de Leeuw, N.H.; Ababii, N.; Carreira, J.F.C.; Rodrigues, J.; Sedrine, N.B.; et al. Nanosensors: Multifunctional Materials: A Case Study of the Effects of Metal Doping on ZnO Tetrapods with Bismuth and Tin Oxides. *Adv Funct. Mater.* **2017**, *27*, 1604676. [[CrossRef](#)]
84. Qiang, X.; Hu, M.; Zhao, B.; Qin, Y.; Yang, R.; Zhou, L.; Qin, Y. Effect of the Functionalization of Porous Silicon/WO<sub>3</sub> Nanorods with Pd Nanoparticles and Their Enhanced NO<sub>2</sub>-Sensing Performance at Room Temperature. *Materials* **2018**, *11*, 764. [[CrossRef](#)] [[PubMed](#)]
85. Ievlev, V.M.; Ryabtsev, S.V.; Samoylov, A.M.; Shaposhnik, A.V.; Kushev, S.B.; Sineelnikov, A.A. Thin and ultrathin films of palladium oxide for oxidizing gases detection. *Sens. Actuators B Chem.* **2018**, *255*, 1335–1342. [[CrossRef](#)]
86. Navale, Y.H.; Navale, S.T.; Ramgir, N.S.; Stadler, F.J.; Gupta, S.K.; Aswal, D.K.; Patil, V.B. Zinc oxide hierarchical nanostructures as potential NO<sub>2</sub> sensors. *Sens. Actuators B Chem.* **2017**, *251*, 551–563. [[CrossRef](#)]
87. Benedict, S.; Singh, M.; Naik, T.R.R.; Shivashankar, S.A.; Bhat, N. Microwave-Synthesized NiO as a Highly Sensitive and Selective Room-Temperature NO<sub>2</sub> Sensor. *ECS J. Solid State Sci. Technol.* **2018**, *7*, Q3143–Q3147. [[CrossRef](#)]
88. Choi, Y.-H.; Kim, D.-H.; Hong, S.-H. CuBi<sub>2</sub>O<sub>4</sub> Prepared by the Polymerized Complex Method for Gas Sensing Applications. *ACS Appl. Mater. Interfaces* **2018**, *10*, 14901–14913. [[CrossRef](#)] [[PubMed](#)]
89. Hung, C.M.; Phuong, H.V.; Duy, N.V.; Hoa, N.D.; Hieu, N.V. Comparative effects of synthesis parameters on the NO<sub>2</sub> gas-sensing performance of on-chip grown ZnO and Zn<sub>2</sub>SnO<sub>4</sub> nanowire sensors. *J. Alloy. Compd.* **2018**, *765*, 1237–1242. [[CrossRef](#)]
90. Aluri, G.S.; Motayed, A.; Davydov, A.V.; Oleshko, V.P.; Bertness, K.A.; Rao, M.V. Nitro-Aromatic Explosive Sensing Using GaN Nanowire-Titania Nanocluster Hybrids. *IEEE Sens. J.* **2013**, *13*, 1883–1888. [[CrossRef](#)]
91. Aluri, G.S.; Motayed, A.; Bertness, K.; Sanford, N.; Oleshko, V.; Davydov, A.; Rao, M.V. Highly selective GaN-nanowire/TiO<sub>2</sub> nanocluster hybrid sensors for detection of benzene and related environmental pollutants. *Nanotechnology* **2011**, *22*, 295503. [[CrossRef](#)] [[PubMed](#)]
92. Aluri, G.S.; Motayed, A.; Davydov, A.V.; Oleshko, V.; Bertness, K.; Sanford, N.; Rao, M.V. GaN-nanowire/TiO<sub>2</sub>-nanocluster hybrid sensors for detection of Benzene and related aromatic compounds. *Proc. SPIE* **2011**, *8024*, 80240M.
93. Aluri, G.S.; Motayed, A.; Bertness, K.; Sanford, N.; Oleshko, V.; Davydov, A.; Rao, M.V. Methanol, Ethanol, and Hydrogen Sensing using Metal-Oxide and Metal (TiO<sub>2</sub>-Pt) Composite Nanoclusters on GaN Nanowires: A New Route towards Tailoring the Selectivity of Nanowire/Nanocluster Chemical Sensors. *Nanotechnology* **2012**, *23*, 17550. [[CrossRef](#)] [[PubMed](#)]

94. Bishop, C.; Salvestrini, J.P.; Halfaya, Y.; Sundaram, S.; el Gmili, Y.; Pradere, L.; Marteau, J.Y.; Assouar, M.B.; Voss, P.L.; Ougazzaden, A. Highly sensitive detection of NO<sub>2</sub> gas using BGaN/GaN superlattice-based double Schottky junction sensors. *Appl. Phys. Lett.* **2015**, *106*, 243504. [[CrossRef](#)]
95. Halfaya, Y.; Bishop, C.; Soltani, A.; Sundaram, S.; Aubry, V.; Voss, P.L.; Salvestrini, J.P.; Ougazzaden, A. Investigation of the Performance of HEMT-Based NO, NO<sub>2</sub> and NH<sub>3</sub> Exhaust Gas Sensors for Automotive Antipollution Systems. *Sensors* **2016**, *16*, 273. [[CrossRef](#)] [[PubMed](#)]
96. Lim, M.; Mills, S.; Lee, B.; Misra, V. Application of AlGaN/GaN Heterostructures for Ultra-Low Power Nitrogen Dioxide Sensing. *ECS J. Solid State Sci. Technol.* **2015**, *4*, S3034–S3037. [[CrossRef](#)]
97. Lv, A.; Pan, Y.; Chi, L. Gas Sensors Based on Polymer Field-Effect Transistors. *Sensors* **2017**, *17*, 213. [[CrossRef](#)] [[PubMed](#)]
98. Kumar, A.; Jha, P.; Singh, A.; Chauhan, A.K.; Gupta, S.K.; Aswal, D.K.; Muthe, K.P.; Gadkari, S.C. Modeling of gate bias controlled NO<sub>2</sub> response of the PCDTBT based organic field effect transistor. *Chem. Phys. Lett.* **2018**, *698*, 7–10. [[CrossRef](#)]
99. Wang, Z.; Huang, L.; Zhu, X.; Zhou, X.; Chi, L. An Ultrasensitive Organic Semiconductor NO<sub>2</sub> Sensor Based on Crystalline TIPS-Pentacene Films. *Adv. Mater.* **2017**, *29*, 1703192. [[CrossRef](#)] [[PubMed](#)]
100. Huang, W.; Zhuang, X.; Melkonyan, F.S.; Wang, B.; Zeng, L.; Wang, G.; Han, S.; Bedzyk, M.J.; Yu, J.; Marks, T.J.; et al. UV–Ozone Interfacial Modification in Organic Transistors for High-Sensitivity NO<sub>2</sub> Detection. *Adv. Mater.* **2017**, *29*, 1701706. [[CrossRef](#)]
101. Niu, Y.; Wang, R.; Jiao, W.; Ding, G.; Hao, L.; Yang, F.; He, X. MoS<sub>2</sub> graphene fiber-based gas sensing devices. *Carbon* **2015**, *95*, 34–41. [[CrossRef](#)]
102. Wang, Z.; Zhang, T.; Zhao, C.; Han, T.; Fei, T.; Liu, S.; Lu, G. Rational synthesis of molybdenum disulfide nanoparticles decorated reduced graphene oxide hybrids and their application for high-performance NO<sub>2</sub> sensing. *Sens. Actuators B Chem.* **2018**, *260*, 508–518. [[CrossRef](#)]
103. Wang, J.; Li, X.; Xia, Y.; Komarneni, S.; Chen, H.; Xu, J.; Xiang, L.; Xie, D. Hierarchical ZnO Nanosheet-Nanorod Architectures for Fabrication of Poly(3-hexylthiophene)/ZnO Hybrid NO<sub>2</sub> Sensor. *ACS Appl. Mater. Interfaces* **2016**, *8*, 8600–8607. [[CrossRef](#)] [[PubMed](#)]
104. Wang, Z.; Zhao, C.; Han, T.; Zhang, Y.; Liu, S.; Fei, T.; Lu, G.; Zhang, T. High-performance reduced graphene oxide-based room-temperature NO<sub>2</sub> sensors: A combined surface modification of SnO<sub>2</sub> nanoparticles and nitrogen doping approach. *Sens. Actuators B Chem.* **2017**, *242*, 269–279. [[CrossRef](#)]
105. Kim, H.W.; Na, H.G.; Kwon, Y.J.; Kang, S.Y.; Choi, M.S.; Bang, J.H.; Wu, P.; Kim, S.S. Microwave-Assisted Synthesis of Graphene-SnO<sub>2</sub> Nanocomposites and Their Applications in Gas Sensors. *ACS Appl. Mater. Interfaces* **2017**, *9*, 31667–31682. [[CrossRef](#)] [[PubMed](#)]
106. Tammanoon, N.; Wisitsoraat, A.; Sriprachubwong, C.; Phokharatkul, D.; Tuantranont, A.; Phanichphant, S.; Liewhiran, C. Ultrasensitive NO<sub>2</sub> Sensor Based on Ohmic Metal-Semiconductor Interfaces of Electrolytically Exfoliated Graphene/Flame-Spray-Made SnO<sub>2</sub> Nanoparticles Composite Operating at Low Temperatures. *ACS Appl. Mater. Interfaces* **2015**, *7*, 24338–24352. [[CrossRef](#)] [[PubMed](#)]
107. Bai, S.; Guo, J.; Sun, J.; Tang, P.; Chen, A.; Luo, R.; Li, D. Enhancement of NO<sub>2</sub>-Sensing Performance at Room Temperature by Graphene-Modified Polythiophene. *Ind. Eng. Chem. Res.* **2016**, *55*, 5788–5794. [[CrossRef](#)]
108. Kwon, Y.J.; Kang, S.Y.; Wu, P.; Peng, Y.; Kim, S.S.; Kim, H.W. Selective Improvement of NO<sub>2</sub> Gas Sensing Behavior in SnO<sub>2</sub> Nanowires by Ion-Beam Irradiation. *ACS Appl. Mater. Interfaces* **2016**, *8*, 13646–13658. [[CrossRef](#)] [[PubMed](#)]
109. Kumar, R.; Goel, N.; Kumar, M. UV-Activated MoS<sub>2</sub> Based Fast and Reversible NO<sub>2</sub> Sensor at Room Temperature. *ACS Sens.* **2017**, *2*, 1744–1752. [[CrossRef](#)] [[PubMed](#)]
110. Liu, J.; Li, S.; Zhang, B.; Xiao, Y.; Gao, Y.; Yang, Q.; Wang, Y.; Lu, G. Ultrasensitive and low detection limit of nitrogen dioxide gas sensor based on flower-like ZnO hierarchical nanostructure modified by reduced graphene oxide. *Sens. Actuators B Chem.* **2017**, *249*, 715–724. [[CrossRef](#)]
111. Long, H.; Trochimczyk, A.H.; Pham, T.; Zettl, A.; Carraro, C.; Worsley, M.A.; Maboudian, R. High Surface Area 3D MoS<sub>2</sub>/Graphene Hybrid Aerogel for Ultrasensitive NO<sub>2</sub> Detection. *Adv. Funct. Mater.* **2016**, *26*, 5158–5165. [[CrossRef](#)]
112. Betty, C.A.; Choudhury, S.; Arora, S. Tin oxide–polyaniline heterostructure sensors for highly sensitive and selective detection of toxic gases at room temperature. *Sens. Actuators B Chem.* **2015**, *220*, 288–294. [[CrossRef](#)]

113. Yang, Y.; Li, S.; Yang, W.; Yuan, W.; Xu, J.; Jiang, Y. In Situ Polymerization Deposition of Porous Conducting Polymer on Reduced Graphene Oxide for Gas Sensor. *ACS Appl. Mater. Interfaces* **2014**, *6*, 13807–13814. [[CrossRef](#)] [[PubMed](#)]
114. Popp, A.; Yilmazoglu, O.; Kaldirim, O.; Schneider, J.J.; Pavlidis, D. A self-supporting monolith of highly aligned carbon nanotubes as device structure for sensor applications. *Chem. Comm.* **2009**, *22*, 3205–3207. [[CrossRef](#)] [[PubMed](#)]
115. Zouaghi, W.; Hussein, L.; Tomson, M.D.; Islam, Q.; Nicoloso, N.; Heinlein, T.; Engstler, J.; Schneider, J.J.; Roskos, H.G. Towards gas sensing with vertically aligned carbon nanotubes interrogated by thz radiation pulses. *Lith. J. Phys.* **2018**, *58*, 38–48. [[CrossRef](#)]
116. Petryshak, V.; Mikityuk, Z.; Vistak, M.; Gotra, Z.; Akhmetova, A.; Wójcik, W.; Assembay, A. Highly sensitive active medium of primary converter SO<sub>2</sub> sensors based on cholesteric-nematic mixtures, doped by carbon nanotubes. *Przeglad Elektrotech.* **2017**, *1*, 119–122. [[CrossRef](#)]
117. Zhang, D.; Liu, J.; Jiang, C.; Li, P.; Sun, Y. High-performance sulfur dioxide sensing properties of layer-by-layer self-assembled titania-modified graphene hybrid nanocomposite. *Sens. Actuators B Chem.* **2017**, *245*, 560–567. [[CrossRef](#)]
118. Eranna, G.; Joshi, B.C.; Runthala, D.P.; Gupta, R.P. Oxide Materials for Development of Integrated Gas Sensors—A Comprehensive Review. *Crit. Rev. Solid State Mater. Sci.* **2004**, *29*, 111–188. [[CrossRef](#)]
119. West, D.L.; Montgomery, F.C.; Armstrong, B.L. Compact, DC-electrical biased sulfur dioxide sensing elements for use at high temperatures. *Sens. Actuators B Chem.* **2012**, *162*, 409–417. [[CrossRef](#)]
120. Liu, Y.; Xu, X.; Chen, Y.; Zhang, Y.; Gao, X.; Xu, P.; Li, X.; Fang, J.; Wen, W. An integrated micro-chip with Ru/Al<sub>2</sub>O<sub>3</sub>/ZnO as sensing material for SO<sub>2</sub> detection. *Sens. Actuators B Chem.* **2018**, *262*, 26–34. [[CrossRef](#)]
121. Ciftiyürek, E.; Sabolsky, K.; Sabolsky, E.M. Molybdenum and tungsten oxide-based gas sensors for high temperature detection of environmentally hazardous sulfur species. *Sens. Actuators B Chem.* **2016**, *237*, 262–274. [[CrossRef](#)]
122. Tyagi, P.; Sharma, A.; Tomar, M.; Gupta, V. Metal oxide catalyst assisted SnO<sub>2</sub> thin film based SO<sub>2</sub> gas sensor. *Sens. Actuators B Chem.* **2016**, *224*, 282–289. [[CrossRef](#)]
123. Haridas, D.; Chowdhuri, A.; Sreenivas, K.; Gupta, V. Effect of thickness of platinum catalyst clusters on response of SnO<sub>2</sub> thin film sensor for LPG. *Sens. Actuators B Chem.* **2011**, *153*, 89–95. [[CrossRef](#)]
124. Das, S.; Rana, S.; Mursalin, S.M.; Rana, P.; Sen, A. Sonochemically prepared nanosized BiFeO<sub>3</sub> as novel SO<sub>2</sub> sensor. *Sens. Actuators B Chem.* **2015**, *218*, 122–127. [[CrossRef](#)]
125. Stephen, J.P.; Cammy, R.A.; Ren, F. *Gallium Nitride Processing for Electronics, Sensors and Spintronics*, 1st ed.; Springer: London, UK, 2006.
126. Anderson, T.; Ren, F.; Pearton, S.; Kang, B.S.; Wang, H.-T.; Chang, C.-Y.; Lin, J. Advances in Hydrogen, Carbon Dioxide, and Hydrocarbon Gas Sensor Technology Using GaN and ZnO-Based Devices. *Sensors* **2009**, *9*, 4669–4694. [[CrossRef](#)] [[PubMed](#)]
127. Triet, N.M.; Duy, L.T.; Hwang, B.-U.; Hanif, A.; Siddiqui, S.; Park, K.; Cho, C.; Lee, N. High-Performance Schottky Diode Gas Sensor Based on the Heterojunction of Three-Dimensional Nanohybrids of Reduced Graphene Oxide-Vertical ZnO Nanorods on an AlGaN/GaN Layer. *ACS Appl. Mater. Interfaces* **2017**, *9*, 30722–30732. [[CrossRef](#)]
128. Jeong, H.Y.; Lee, D.-S.; Choi, H.K.; Lee, D.H.; Kim, J.-E.; Lee, J.Y.; Lee, W.J.; Kim, S.O.; Choi, S.-Y. Flexible Room-Temperature NO<sub>2</sub> Gas Sensors Based on Carbon Nanotubes/Reduced Graphene Hybrid Films. *Appl. Phys. Lett.* **2010**, *96*, 213105. [[CrossRef](#)]
129. Wang, L.; Kumar, R.V. A SO<sub>2</sub> gas sensor based upon composite NASICON/Sr–Al<sub>2</sub>O<sub>3</sub> bielectrolyte. *Mater. Res. Bull.* **2005**, *40*, 1802–1815. [[CrossRef](#)]
130. Saganuma, S.; Watanabe, M.; Kobayashi, T.; Wakabayashi, S. SO<sub>2</sub> gas sensor utilizing stabilized zirconia and sulfate salts with a new working mechanism. *Solid State Ionics* **1999**, *126*, 175–179. [[CrossRef](#)]
131. Wang, L.; Kumar, R.V. A new SO<sub>2</sub> gas sensor based on an Mg<sup>2+</sup> conducting solid electrolyte. *J. Electroanal. Chem.* **2003**, *543*, 109–114. [[CrossRef](#)]
132. Ma, C.; Hao, X.; Yang, X.; Liang, X.; Liu, F.; Liu, T.; Yang, C.; Zhu, H.; Lu, G. Sub-ppb SO<sub>2</sub> gas sensor based on NASICON and La<sub>x</sub>Sm<sub>1-x</sub>FeO<sub>3</sub> sensing electrode. *Sens. Actuators B Chem.* **2018**, *256*, 648–655. [[CrossRef](#)]
133. Liu, F.; Wang, Y.; Wang, B.; Yang, X.; Wang, Q.; Liang, X.; Sun, P.; Chuai, X.; Wang, Y.; Lu, G. Stabilized zirconia-based mixed potential type sensors utilizing MnNb<sub>2</sub>O<sub>6</sub> sensing electrode for detection of low-concentration SO<sub>2</sub>. *Sens. Actuators B Chem.* **2017**, *238*, 1024–1031. [[CrossRef](#)]

134. Auerbach, S.M.; Carrado, K.A.; Dutta, P.K. *Handbook of Zeolite Science and Technology*; Marcel Dekker, Inc.: New York, NY, USA, 2003.
135. Yimlamai, I.; Niamlang, S.; Chanthanont, P.; Kunanuraksapong, R.; Changkhamchom, S.; Sirivat, A. Electrical conductivity response and sensitivity of ZSM-5, Y, and mordenite zeolites towards ethanol vapor. *Ionics* **2011**, *17*, 607–615. [[CrossRef](#)]
136. Choeichom, P.; Sirivat, A. Discriminative sensing performances of ZSM-5, Y, mordenite, ferrierite, beta, 3A, 4A, 5A, and 13X zeolites towards sulfur dioxide. *Ionics* **2018**, *24*, 2829–2841. [[CrossRef](#)]
137. Li, Q.; Wu, J.; Huang, L.; Gao, J.; Zhou, H.; Shi, Y.; Pan, Q.; Zhang, G.; Du, Y.; Liang, W. Sulfur dioxide gas-sensitive materials based on zeolitic imidazolate framework-derived carbon nanotubes. *J. Mater. Chem. A* **2018**, *6*, 12115–12124. [[CrossRef](#)]
138. Chanthanont, P.; Permpool, T.; Sirivat, A. Effect of alkaline and alkaline earth ion exchanged Y zeolites on electrical conductivity and response of PEDOT-PSS/Y zeolite composites toward SO<sub>2</sub>. *Mater. Technol.* **2015**, *30*, 193–199. [[CrossRef](#)]
139. Lim, S.H.; Feng, L.; Kemling, J.W.; Musto, C.J.; Suslick, K.S. An Optoelectronic Nose for Detection of Toxic Gases. *Nat. Chem.* **2009**, *1*, 562–567. [[CrossRef](#)] [[PubMed](#)]
140. Martinez, A.W.; Phillips, S.T.; Whitesides, G.M.; Carrilho, E. Diagnostics for the developing world: Microfluidic paper-based analytical devices. *Anal. Chem.* **2010**, *82*, 3–10. [[CrossRef](#)] [[PubMed](#)]
141. Li, D.; Duan, H.; Ma, Y.; Deng, W. Headspace-Sampling Paper-Based Analytical Device for Colorimetric/Surface-Enhanced Raman Scattering Dual Sensing of Sulfur Dioxide in Wine. *Anal. Chem.* **2018**, *90*, 5719–5727. [[CrossRef](#)]
142. Wang, M.; Guo, L.; Cao, D. Amino-Functionalized Luminescent Metal-Organic Framework Test Paper for Rapid and Selective Sensing of SO<sub>2</sub> Gas and Its Derivatives by Luminescence Turn-On Effect. *Anal. Chem.* **2018**, *90*, 3608–3614. [[CrossRef](#)]
143. Liu, C.-C.; Wang, Y.-N.; Fu, L.-M.; Yang, D.-Y. Rapid integrated microfluidic paper-based system for sulfur dioxide detection. *Chem. Eng. J.* **2017**, *316*, 790–796. [[CrossRef](#)]
144. Chaudhary, V.; Kaur, A. Solitary surfactant assisted morphology dependent chemiresistive polyaniline sensors for room temperature monitoring of low parts per million sulfur di oxide. *Polym. Int.* **2015**, *64*, 1475–1481. [[CrossRef](#)]
145. Chaudhary, V.; Kaur, A. Enhanced room temperature sulfur dioxide sensing behaviour of in situ polymerized polyaniline-tungsten oxide nanocomposite possessing honeycomb morphology. *RSC Adv.* **2015**, *5*, 73535–73544. [[CrossRef](#)]
146. Betty, C.A.; Choudhury, S. Charge carrier transport in nanocrystalline SnO<sub>2</sub> thin film sensor and temperature dependence of toxic gas sensitivity. *Sens. Actuators B Chem.* **2016**, *237*, 787–794. [[CrossRef](#)]
147. Gaiardo, A.; Fabbri, B.; Giberti, A.; Guidi, V.; Bellutti, P.; Malagù, C.; Valt, M.; Pepponi, G.; Gherardi, S.; Zonta, G.; et al. ZnO and Au/ZnO thin films: Room-temperature chemoresistive properties for gas sensing applications. *Sens. Actuators B Chem.* **2016**, *237*, 1085–1094. [[CrossRef](#)]
148. Wang, H.; Liu, Z.; Chen, D.; Jiang, Z. A new potentiometric SO<sub>2</sub> sensor based on Li<sub>3</sub>PO<sub>4</sub> electrolyte film and its response characteristics. *Rev. Sci. Instrum.* **2015**, *86*, 075007. [[CrossRef](#)] [[PubMed](#)]
149. Mulmi, S.; Thangadurai, V. Semiconducting SnO<sub>2</sub>-TiO<sub>2</sub> (ST) composites for detection of SO<sub>2</sub> gas. *Ionics* **2016**, *22*, 1927–1935. [[CrossRef](#)]
150. Chen, A.M.; Liu, R.; Peng, X.; Chen, Q.; Wu, J. 2D Hybrid Nanomaterials for Selective Detection of NO<sub>2</sub> and SO<sub>2</sub> Using “Light On and Off” Strategy. *ACS Appl. Mater. Interfaces* **2017**, *9*, 37191. [[CrossRef](#)]
151. Chaudhary, V.; Singh, H.K.; Kaur, A. Effect of charge carrier transport on sulfur dioxide monitoring performance of highly porous polyaniline nanofibers. *Polym. Int.* **2017**, *66*, 699. [[CrossRef](#)]
152. Ovsianytskyi, O.; Nam, Y.-S.; Tsybalenko, O.; Lan, P.; Moon, M.; Lee, K. Highly sensitive chemiresistive H<sub>2</sub>S gas sensor based on graphene decorated with Ag nanoparticles and charged impurities. *Sens. Actuators B Chem.* **2018**, *257*, 278–285. [[CrossRef](#)]
153. Chu, J.; Wang, X.; Wang, D.; Yang, A.; Lv, P.; Wu, Y.; Rong, M.; Gao, L. 3 Highly selective detection of sulfur hexafluoride decomposition components H<sub>2</sub>S and SOF<sub>2</sub> employing sensors based on tin oxide modified reduced graphene oxide. *Carbon* **2018**, *135*, 95–103. [[CrossRef](#)]
154. Zhang, J.; Zhu, Z.; Chen, C. ZnO-carbon nanofibers for stable, high response, and selective H<sub>2</sub>S sensors. *Nanotechnology* **2018**, *29*, 275501. [[CrossRef](#)]

155. Sokolovskij, R.; Zhangb, J.; Iervolino, E.; Zhao, C.; Santagata, F.; Wang, F.; Yu, H.; Sarro, P.M.; Zhang, G.Q. Hydrogen sulfide detection properties of Pt-gated AlGa<sub>N</sub>/Ga<sub>N</sub> HEMT-sensor. *Sens. Actuators B Chem.* **2018**, *274*, 636–644. [[CrossRef](#)]
156. Lo, C.-F.; Xi, Y.; Liu, L.; Pearton, S.J.; Doré, S.; Hsu, C.-H.; Dabiran, A.M.; Chow, P.P.; Ren, F. Effect of temperature on CO sensing response in air ambient by using ZnO nanorod-gated AlGa<sub>N</sub>/Ga<sub>N</sub> high electron mobility transistors. *Sens. Actuators B Chem.* **2013**, *176*, 708–712. [[CrossRef](#)]
157. Chen, T.Y.; Chen, H.I.; Hsu, C.S.; Huang, C.C.; Chang, C.F.; Chou, P.C.; Liu, W.C. On an Ammonia gas sensor based on a Pt/AlGa<sub>N</sub> heterostructure field-effect transistor. *IEEE Electron Device Lett.* **2012**, *33*, 612–614.
158. Son, K.A.; Yang, B.; Prokopuk, N.; Moon, J.S.; Liao, A.; Katona, T.M.; Khan, M.A. RF Ga<sub>N</sub> HEMT sensors for detection of caustic chemicals. *IEEE Sens. J.* **2011**, *11*, 3476–3478. [[CrossRef](#)]
159. Zhanga, J.; Sokolovskijb, R.; Chen, G.; Zhu, Y.; Qi, Y.; Lin, X.; Li, W.; Zhang, G.Q.; Jiang, Y.; Yu, H. Impact of high temperature H<sub>2</sub> pre-treatment on Pt-AlGa<sub>N</sub>/Ga<sub>N</sub> HEMT sensor for H<sub>2</sub>S detection. *Sens. Actuators B Chem.* **2018**, *280*, 138–143. [[CrossRef](#)]
160. Shukla, G.P.; Bhatnagar, M.C. H<sub>2</sub>S gas sensor based on Cu doped SnO<sub>2</sub> nanostructure. *J. Mater. Sci. Eng. A* **2014**, *4*. [[CrossRef](#)]
161. Hosseini, Z.S.; zad, A.I.; Mortezaali, A. Room temperature (24.0 ± 1 °C) H<sub>2</sub>S gas sensor based on rather aligned ZnO nanorods with flower-like structures. *Sens. Actuators B Chem.* **2015**, *207*, 865–871. [[CrossRef](#)]
162. Li, Z.; Huang, Y.; Zhang, S.; Chen, W.; Kuang, Z.; Ao, D.; Liu, W.; Fu, Y. A fast response & recovery H<sub>2</sub>S gas sensor based on α-Fe<sub>2</sub>O<sub>3</sub> nanoparticles with ppb level detection limit. *J. Hazard. Mater.* **2015**, *300*, 167–174. [[PubMed](#)]
163. Zhang, H.-J.; Meng, F.-N.; Liu, L.-Z.; Chen, Y.-J. Convenient route for synthesis of alpha-Fe<sub>2</sub>O<sub>3</sub> and sensors for H<sub>2</sub>S gas. *J. Alloy. Compd.* **2019**, *774*, 1181–1188. [[CrossRef](#)]
164. Li, D.; Qin, L.; Zhao, P.; Zhang, Y.; Liu, D.; Liu, F.; Kang, B.; Wang, Y.; Song, H.; Zhang, T.; et al. Preparation and gas-sensing performances of ZnO/CuO rough nanotubular arrays for low-working temperature H<sub>2</sub>S detection. *Sens. Actuators B Chem.* **2018**, *254*, 834–841. [[CrossRef](#)]
165. Li, Z.; Yan, S.; Zhang, S.; Wang, J.; Shen, W.; Wang, Z.; Fu, Y.Q. Ultra-sensitive UV and H<sub>2</sub>S dual functional sensors based on porous In<sub>2</sub>O<sub>3</sub> nanoparticles operated at room temperature. *J. Alloy. Compd.* **2019**, *770*, 721–731. [[CrossRef](#)]
166. Huang, H.; Xu, P.; Zheng, D.; Chen, C.; Li, X. Sulfuration-desulfuration reaction sensing-effect of intrinsic ZnO nanowires for high-performance H<sub>2</sub>S detection. *J. Mater. Chem. A* **2015**, *3*, 6330–6339. [[CrossRef](#)]
167. Eoma, N.S.A.; Chob, H.-B.; Song, Y.; Go, G.M.; Lee, J.; Choa, Y. Room-temperature H<sub>2</sub>S gas sensing by selectively synthesized Cu<sub>x(x=1,2)</sub>O:SnO<sub>2</sub> thin film nanocomposites with oblique & vertically assembled SnO<sub>2</sub> ceramic nanorods. *Sens. Actuators B Chem.* **2018**, *273*, 1054–1061.
168. Stanoiu, A.; Piticescu, R.M.; Simion, C.E.; Rusti-Ciobota, C.; Florea, O.; Teodorescu, V.; Osiceanu, P.; Sobetkii, A.; Badilita, V. H<sub>2</sub>S selective sensitivity of Cu doped BaSrTiO<sub>3</sub> under operando conditions and the associated sensing mechanism. *Sens. Actuators B Chem.* **2018**, *264*, 327–336. [[CrossRef](#)]
169. Quang, P.L.; Cuong, N.D.; Hoa, T.T.; Long, H.T.; Hung, C.M.; Le, D.T.T.; Hieu, N.V. Simple post-synthesis of mesoporous p-type Co<sub>3</sub>O<sub>4</sub> nanochains for enhanced H<sub>2</sub>S gas sensing performance. *Sens. Actuators B Chem.* **2018**, *270*, 158–166. [[CrossRef](#)]
170. Stanoiu, A.; Simion, C.E.; Calderon-Moreno, J.M.; Osiceanu, P.; Florea, M.; Teodorescu, V.S.; Somacescu, S. Sensors based on mesoporous SnO<sub>2</sub>-CuWO<sub>4</sub> with high selective sensitivity to H<sub>2</sub>S at low operating temperature. *J. Hazard. Mater.* **2017**, *331*, 150–160. [[CrossRef](#)] [[PubMed](#)]
171. Hu, X.; Zhu, Z.; Li, Z.; Xie, L.; Wu, Y.; Zheng, L. Heterostructure of CuO microspheres modified with CuFe<sub>2</sub>O<sub>4</sub> nanoparticles for highly sensitive H<sub>2</sub>S gas sensor. *Sens. Actuators B Chem.* **2018**, *264*, 139–149. [[CrossRef](#)]
172. Li, H.; Li, J.; Zhu, Y.; Xie, W.; Shao, R.; Yao, X.; Gao, A.; Yin, Y. Cd<sup>2+</sup>-Doped Amorphous TiO<sub>2</sub> Hollow Spheres for Robust and Ultrasensitive Photoelectrochemical Sensing of Hydrogen Sulfide. *Anal. Chem.* **2018**, *90*, 5496–5502. [[CrossRef](#)]
173. Yassine, O.; Shekhah, O.; Assen, A.H.; Belmabkhout, Y.; Salama, K.N.; Eddaoudi, M. H<sub>2</sub>S sensors: Fumarate-based fcu-MOF thin film grown on a capacitive interdigitated electrode. *Angew. Chem. Int. Ed.* **2016**, *55*, 15879–15883. [[CrossRef](#)]
174. Guo, L.; Wang, M.; Cao, D. A Novel Zr-MOF as Fluorescence Turn-On Probe for Real-Time Detecting H<sub>2</sub>S Gas and Fingerprint Identification. *Small* **2018**, *14*, 1703822. [[CrossRef](#)]

175. Dong, X.; Su, Y.; Lu, T.; Zhang, L.; Wu, L.; Lv, Y. MOFs-derived dodecahedra porous  $\text{Co}_3\text{O}_4$ : An efficient cataluminescence sensing material for  $\text{H}_2\text{S}$ . *Sens. Actuators B Chem.* **2018**, *258*, 349–357. [[CrossRef](#)]
176. Chaudhary, N.; Singh, A.; Debnath, A.K.; Acharya, S.; Aswal, D.K. Electron beam modified organic materials and their applications. *Solid State Phenom.* **2015**, *239*, 72–97. [[CrossRef](#)]
177. Chaudhary, N.; Singh, A.; Aswal, D.K.; Jha, P.; Samanta, S.; Chauhan, A.; Debnath, A.; Acharya, S.; Shah, K.; Muthe, K.; et al. Electron beam induced modifications of polyaniline silver nano-composite films: Electrical conductivity and  $\text{H}_2\text{S}$  gas sensing studies. *Radiat. Phys. Chem.* **2018**, *153*, 131–139. [[CrossRef](#)]
178. Abu-Hani, A.F.; Greish, Y.E.; Mahmoud, S.T.; Awwad, F.; Ayeshe, A.I. Low-temperature and fast response  $\text{H}_2\text{S}$  gas sensor using semiconducting chitosan film. *Sens. Actuators B Chem.* **2017**, *253*, 677–684. [[CrossRef](#)]
179. Shu, J.; Qiu, Z.; Lv, S.; Zhang, K.; Tang, D.  $\text{Cu}^{2+}$ -Doped  $\text{SnO}_2$  Nanograin/Poly pyrrole Nanospheres with Synergic Enhanced Properties for Ultrasensitive Room-Temperature  $\text{H}_2\text{S}$  Gas Sensing. *Anal. Chem.* **2017**, *89*, 11135–11142. [[CrossRef](#)] [[PubMed](#)]
180. Hao, X.; Ma, C.; Yang, X.; Liu, T.; Wang, B.; Liu, F.; Liang, X.; Yang, C.; Zhu, H.; Lu, G. YSZ-based mixed potential  $\text{H}_2\text{S}$  sensor using  $\text{La}_2\text{NiO}_4$  sensing electrode. *Sens. Actuators B Chem.* **2018**, *255*, 3033–3039. [[CrossRef](#)]
181. Yang, X.; Zhang, Y.; Hao, X.; Song, Y.; Liang, X.; Liu, F.; Sun, P.; Gao, Y.; Yan, X.; Lu, G. Nafion-based amperometric  $\text{H}_2\text{S}$  sensor using Pt Rh/C sensing electrode. *Sens. Actuators B Chem.* **2018**, *273*, 635–641. [[CrossRef](#)]
182. Asres, G.A.; Baldoví, J.J.; Dombovari, A.; Järvinen, T.; Lorite, G.S.; Mohl, M.; Shchukarev, A.; Paz, A.P.; Xian, L.; Mikkola, J.; et al. Ultrasensitive  $\text{H}_2\text{S}$  gas sensors based on p-type  $\text{WS}_2$  hybrid materials. *Nano Res.* **2018**, *11*, 4215–4224. [[CrossRef](#)]
183. Zhou, C.; Yang, W.; Zhu, H. Mechanism of charge transfer and its impacts on Fermi-level pinning for gas molecules adsorbed on monolayer  $\text{WS}_2$ . *J. Chem. Phys.* **2015**, *142*, 214704. [[CrossRef](#)] [[PubMed](#)]
184. Kaur, M.; Jain, N.; Sharma, K.; Bhattacharya, S.; Roy, M.; Tyagi, A.K.; Gupta, S.K.; Yakhmi, J.V. Room temperature  $\text{H}_2\text{S}$  gas sensing at ppb level by single crystal  $\text{In}_2\text{O}_3$  whiskers. *Sens. Actuator. B Chem.* **2008**, *133*, 456–461. [[CrossRef](#)]
185. Yang, M.; Zhang, X.; Cheng, X.; Xu, Y.; Gao, S.; Zhao, H.; Huo, L. Hierarchical NiO Cube/Nitrogen-Doped Reduced Graphene Oxide Composite with Enhanced  $\text{H}_2\text{S}$  Sensing Properties at Low Temperature. *ACS Appl. Mater. Interfaces* **2017**, *9*, 26293–26303. [[CrossRef](#)]
186. Shi, J.; Cheng, Z.; Gao, L.; Zhang, Y.; Xu, J.; Zhao, H. Facile synthesis of reduced graphene oxide/hexagonal  $\text{WO}_3$  nanosheets composites with enhanced  $\text{H}_2\text{S}$  sensing properties. *Sens. Actuators B Chem.* **2016**, *230*, 736–745. [[CrossRef](#)]
187. Balouria, V.; Ramgir, N.S.; Singh, A.; Debnath, A.K.; Mahajan, A.; Bedi, R.K.; Aswal, D.K.; Gupta, S.K. Enhanced  $\text{H}_2\text{S}$  sensing characteristics of Au modified  $\text{Fe}_2\text{O}_3$  thin films. *Sens. Actuators B Chem.* **2015**, *219*, 125–132. [[CrossRef](#)]
188. Li, Z.J.; Lin, Z.J.; Wang, N.N.; Huang, Y.W.; Wang, J.Q.; Liu, W.; Fu, Y.Q.; Wang, Z.G. Facile synthesis of  $\alpha\text{-Fe}_2\text{O}_3$  micro-ellipsoids by surfactant-free hydrothermal method for sub-ppm level  $\text{H}_2\text{S}$  detection. *Mater. Des.* **2016**, *110*, 532–539. [[CrossRef](#)]
189. Kheel, H.; Sun, G.J.; Lee, J.K.; Lee, S.; Dwivedi, R.P.; Lee, C. Enhanced  $\text{H}_2\text{S}$  sensing performance of  $\text{TiO}_2$ -decorated  $\alpha\text{-Fe}_2\text{O}_3$  nanorod sensors. *Ceram. Int.* **2016**, *42*, 18597–18604. [[CrossRef](#)]
190. Benedict, S.; Lumdee, C.; Dmitriev, A.; Anand, S.; Bhat, N. Colloidal lithography nanostructured Pd/PdO<sub>x</sub> core-shell sensor for ppb level  $\text{H}_2\text{S}$  detection. *Nanotechnology* **2018**, *29*, 255502. [[CrossRef](#)]
191. Gao, X.; Sun, Y.; Zhu, C.; Li, C.; Ouyang, Q.; Chen, Y. Highly sensitive and selective  $\text{H}_2\text{S}$  sensor based on porous  $\text{ZnFe}_2\text{O}_4$  nanosheets. *Sens. Actuators B Chem.* **2017**, *246*, 662–672. [[CrossRef](#)]
192. Fu, D.; Zhu, C.; Zhang, X.; Li, C.; Chen, Y. Two-dimensional net-like  $\text{SnO}_2/\text{ZnO}$  heteronanostructures for high-performance  $\text{H}_2\text{S}$  gas sensor. *J. Mater. Chem. A* **2016**, *4*, 1390–1398. [[CrossRef](#)]
193. Gao, C.; Lin, Z.-D.; Li, N.; Fu, P.; Wang, X.-H. Preparation and  $\text{H}_2\text{S}$  Gas-Sensing Performances of Coral Like  $\text{SnO}_2\text{-CuO}$  Nanocomposite. *Acta Metall. Sin. (Engl. Lett.)* **2015**, *28*, 1190–1197. [[CrossRef](#)]
194. Wang, Y.; Qu, F.; Liu, J.; Wang, Y.; Zhou, J.; Ruan, S. Enhanced  $\text{H}_2\text{S}$  sensing characteristics of CuO-NiO core-shell microspheres sensors. *Sens. Actuators B Chem.* **2015**, *209*, 515–523. [[CrossRef](#)]
195. Wang, Y.; Liu, B.; Xiao, S.; Wang, X.; Sun, L.; Li, H.; Xie, W.; Li, Q.; Zhang, Q.; Wang, T. Low-Temperature  $\text{H}_2\text{S}$  Detection with Hierarchical Cr-Doped  $\text{WO}_3$  Microspheres. *ACS Appl. Mater. Interfaces* **2016**, *8*, 9674–9683. [[CrossRef](#)]

196. Tian, J.; Pan, F.; Xue, R.; Zhang, W.; Fang, X.; Liu, Q.; Wang, Y.; Zhang, Z.; Zhang, D. A highly sensitive room temperature H<sub>2</sub>S gas sensor based on SnO<sub>2</sub> multi-tube arrays bio-templated from insect bristles. *Dalton Trans.* **2015**, *44*, 7911–7916. [[CrossRef](#)]
197. Yu, T.; Cheng, X.; Zhang, X.; Sui, L.; Xu, Y.; Gao, S.; Zhao, H.; Huo, L. Highly sensitive H<sub>2</sub>S detection sensors at low temperature based on hierarchically structured NiO porous nanowall arrays. *J. Mater. Chem. A* **2015**, *3*, 11991–11999. [[CrossRef](#)]
198. Asad, M.; Sheikhi, M.H.; Pourfath, M.; Moradi, M. High sensitive and selective flexible H<sub>2</sub>S gas sensors based on Cu nanoparticle decorated SWCNTs. *Sens. Actuators B Chem.* **2015**, *210*, 1–8. [[CrossRef](#)]
199. Li, Z.; Wang, N.; Lin, Z.; Wang, J.; Liu, W.; Sun, K.; Fu, Y.Q.; Wang, Z. Room-Temperature High-Performance H<sub>2</sub>S Sensor Based on Porous CuO Nanosheets Prepared by Hydrothermal Method. *ACS Appl. Mater. Interfaces* **2016**, *8*, 20962–20968. [[CrossRef](#)]
200. Su, P.; Peng, Y. Fabrication of a room-temperature H<sub>2</sub>S gas sensor based on ppy/WO<sub>3</sub> nanocomposite films by in-situ photopolymerization. *Sens. Actuator. B Chem.* **2014**, *193*, 637–643. [[CrossRef](#)]
201. Choi, S.; Jang, B.; Lee, S.; Min, B.K.; Rothschild, A.; Kim, I. Selective detection of acetone and hydrogen sulfide for the diagnosis of diabetes and halitosis using SnO<sub>2</sub> nanofibers functionalized with reduced graphene oxide nanosheets. *ACS Appl. Mater. Interface* **2014**, *6*, 2588–2597. [[CrossRef](#)]
202. Chen, X.-P.; Wang, L.-M.; Sun, X.; Meng, R.-S.; Xiao, J.; Ye, H.-Y.; Zhang, G.-Q. Sulfur Dioxide and Nitrogen Dioxide Gas Sensor Based on Arsenene: A First-Principle Study. *IEEE Electron. Device Lett.* **2017**, *38*, 661–664. [[CrossRef](#)]
203. Mao, Y.; Long, L.; Yuan, J.; Zhong, J.; Zhao, H. Toxic gases molecules (NH<sub>3</sub>, SO<sub>2</sub> and NO<sub>2</sub>) adsorption on GeSe monolayer with point defects engineering. *Chem. Phys. Lett.* **2018**, *706*, 501–508. [[CrossRef](#)]
204. Huang, C.-S.; Murat, A.; Babar, V.; Montes, E.; Schwingenschlöggl, U. Adsorption of the Gas Molecules NH<sub>3</sub>, NO, NO<sub>2</sub>, and CO on Borophene. *J. Phys. Chem. C* **2018**, *122*, 14665–14670. [[CrossRef](#)]
205. Cui, H.; Zheng, K.; Zhang, Y.; Ye, H.; Chen, X. Superior Selectivity and Sensitivity of C<sub>3</sub>N Sensor in Probing Toxic Gases NO<sub>2</sub> and SO<sub>2</sub>. *IEEE Electron. Device Lett.* **2018**, *39*, 284–287. [[CrossRef](#)]
206. Niu, F.; Yang, D.; Cai, M.; Li, X.; Liu, D. A First Principles Study of Blue Phosphorene as A Superior Media for Gas Sensor. *ICEPT* **2018**, 1149–1152. [[CrossRef](#)]
207. Ingale, N.; Konda, R.; Chaudhari, A. Organolithium complex as a gas sensing material for oxides from ab initio calculations and molecular dynamics simulations. *Int. J. Quantum Chem.* **2018**, *118*, e25623. [[CrossRef](#)]
208. Wei, H.; Gui, Y.; Kang, J.; Wang, W.; Tang, C. A DFT Study on the Adsorption of H<sub>2</sub>S and SO<sub>2</sub> on Ni Doped MoS<sub>2</sub> Monolayer. *Nanomaterials* **2018**, *8*, 646. [[CrossRef](#)]
209. Hussain, T.; Kaewmaraya, T.; Chakraborty, S.; Vovusha, H.; Amornkitbamrung, V.; Ahuja, R. Defected and Functionalized Germanene-based Nanosensors under Sulfur Comprising Gas Exposure. *ACS Sens.* **2018**, *3*, 867–874. [[CrossRef](#)]
210. Liao, T.; Kou, L.; Du, A.; Chen, L.; Cao, C.; Sun, Z. H<sub>2</sub>S Sensing and Splitting on Atom-Functionalized Carbon Nanotubes: A Theoretical Study. *Adv. Theory Simul.* **2018**, *1*, 1700033. [[CrossRef](#)]
211. Yong, Y.; Su, X.; Cui, H.; Zhou, Q.; Kuang, Y.; Li, X. Two-Dimensional Tetragonal GaN as Potential Molecule Sensors for NO and NO<sub>2</sub> Detection: A First-Principle Study. *ACS Omega* **2017**, *2*, 8888–8895. [[CrossRef](#)]
212. Yong, Y.; Cui, H.; Zhou, Q.; Su, X.; Kuang, Y.; Li, X. Adsorption of gas molecules on a graphitic GaN sheet and its implications for molecule sensors. *RSC Adv.* **2017**, *7*, 51027. [[CrossRef](#)]
213. Spinelle, L.; Alexandre, M.; Gerboles, M. *Protocol of Evaluation and Calibration of Low-Cost Gas Sensors for the Monitoring of air Pollution*; JRC Technical Reports (JRC83791); Publications Office of the European Union: Brussels, Belgium, 2013.
214. Monroy, J.G.; Lilienthal, A.; Blanco, J.L.; González-Jimenez, J.; Trincavelli, M. Calibration of MOX gas sensors in open sampling systems based on Gaussian Processes. *Sensors* **2012**, *2012*, 1–4.
215. Perma Pure, L.L.C. Gas Sensor Calibration, Chapter 11. In *Hazardous Gas Monitors*; Elsevier: Amsterdam, The Netherlands, 2013.
216. Alreshaid, A.T.; Hester, J.G.; Su, W.; Fang, Y.; Tentzeris, M.M. Review—Ink-Jet Printed Wireless Liquid and Gas Sensors for IoT, SmartAg and Smart City Applications. *J. Electrochem. Soc.* **2018**, *165*, B407–B413. [[CrossRef](#)]
217. Ramaswamy, P. IoT smart parking system for reducing green-house gas emission. In Proceedings of the 2016 International Conference on Recent Trends in Information Technology (ICRTIT), Chennai, India, 8–9 April 2016; pp. 1–6.

218. Suh, J.H.; Cho, I.; Kang, K.; Kweon, S.-J.; Lee, M.; Yoo, H.-J.; Park, I. Fully integrated and portable semiconductor-type multi-gas sensing module for IoT applications. *Sens. Actuators B Chem.* **2018**, *265*, 660–667. [[CrossRef](#)]
219. Ashokkumar, M.; Thirumurugan, T. Integrated IOT based design and Android operated Multi-purpose Field Surveillance Robot for Military Use. In *Advances in Engineering Research, Proceedings of the International Conference for Phoenixes on Emerging Current Trends in Engineering and Management (PECTEAM 2018), 9–10 February 2018, Chennai, India*; Atlantis Press: Paris, France, 2018; Volume 142, pp. 236–243.
220. Rushikesh, R.; Sivappagari, C.M.R. Development of IoT based vehicular pollution monitoring system. In *Proceedings of the 2015 International Conference on Green Computing and Internet of Things (ICGCIoT), Noida, India, 8–10 October 2015*; pp. 779–783.
221. Shu, L.; Mukherjee, M.; Wu, X. Toxic gas boundary area detection in large-scale petrochemical plants with industrial wireless sensor networks. *IEEE Commun. Mag.* **2016**, *54*, 22–28. [[CrossRef](#)]
222. Alcantara, G.P. A short review of gas sensors based on interdigital electrode. *IEEE ICEMI* **2015**, *12*, 1616–1621.



© 2019 by the authors. Licensee MDPI, Basel, Switzerland. This article is an open access article distributed under the terms and conditions of the Creative Commons Attribution (CC BY) license (<http://creativecommons.org/licenses/by/4.0/>).